Aerosol layer height (ALH) retrievals from oxygen absorption bands: Intercomparison and validation among different satellite platforms, GEMS, EPIC, and TROPOMI

Hyerim Kim[1], Xi Chen[1], Jun Wang[1,2], Zhendong Lu[2], Meng Zhou[2], Gregory R. Carmichael[1], Sang Seo Park[3], Jhoon Kim[4]

[1]Department of Chemical and Biochemical Engineering, Center for Global and Regional Environmental Research, Iowa Technology Institute, The University of Iowa, Iowa City, 52242, USA
[2]Interdisciplinary Graduate Program in Informatics, The University of Iowa, Iowa City, 52242, USA
[3]School of Urban and Environmental Engineering, Ulsan National Institute of Science and Technology (UNIST), Ulsan 689-798, Republic of Korea
[4]Department of Atmospheric Sciences, Yonsei University, Seoul 03722, South Korea

Correspondence to: Xi Chen (xi-chen-4@uiowa.edu); Jun Wang (jun-wang-1@uiowa.edu)

Abstract.

Although containing only single piece of information, aerosol layer height (ALH) indicates the altitude of aerosol layer in vertical coordinate which is essential for assessment of surface air quality and aerosol climate impact. Passive remote sensing measurements in oxygen (O_2) absorption bands are sensitive to ALH, providing an opportunity to derive global or regional ALH information from satellite observations. In this study, we compare ALH products retrieved from near-infrared O_2 absorption measurements from multiple satellite platforms including Geostationary Environment Monitoring Spectrometer (GEMS) focusing on Asia, Earth Polychromatic Imaging Camera (EPIC) in deep space, and polar orbiting satellite TROPOspheric Monitoring Instrument (TROPOMI), and validate them using spaceborne lidar (CALIOP) measurements for typical dust and smoke plumes. Adjustments have been made to account for the inherent variations in the definitions of ALH among different products, ensuring an apple-to-apple comparison. In comparison with CALIOP ALH, both EPIC and TROPOMI ALH display a high correlation coefficient (R) higher than 0.7 and an overestimation by ~ 0.8 km, whereas GEMS ALH exhibits minimal bias (0.1 km) but a slightly lower correlation with R of 0.64. Categorizing GEMS retrievals with UVAI ≥ 3 improves the agreement with CALIOP. GEMS ALH demonstrates a narrower range and lower mean value compared to EPIC and TROPOMI, and their correlation is further improved when UVAI ≥ 3. Furthermore, diurnal variation of GEMS and EPIC ALH, especially for UVAI ≥ 3, aligns with boundary layer development. Considering the important role of AOD in ALH retrieval, we found GEMS AOD at 680 nm correlates well with AERONET AOD (R ~ 0.9) but features a negative bias of -0.2. EPIC and TROPOMI tend to overestimate AOD by 0.33 km and 0.23 km, respectively, in dust cases. Finally, a dust and a smoke case are analysed in detail to explore the variation of ALH during plume transport from multiple data.

1 Introduction

Atmospheric aerosols influence the Earth's energy budget and climate system by absorbing and scattering solar and terrestrial radiation ((Wang and Christopher, 2003). The aerosol vertical distribution is one of the most important factors determining the

35   aerosol radiative effects (Zhang et al., 2013). The altitude of absorbing aerosols such as dust and smoke affect the vertical distribution of radiative heating and modify the stability of the atmosphere (Babu et al., 2011; Koch and Del Genio, 2010; Wendisch et al., 2008; Wang and Christopher, 2006). When aerosols are lifted to high altitudes in upper troposphere and lower stratosphere, they can have longer residence times and transport over longer distance, influencing global radiative energy budget (Christian et al., 2019; Peterson et al., 2014). Aerosol vertical distribution influence the derivation of aerosol optical

40   properties, such as AOD and single scattering albedo in the UV spectrum where the top-of-atmosphere (TOA) radiance is also sensitive to the vertical variation of aerosols (Torres et al., 1998). Furthermore, estimates of surface concentration of particulate matter (PM) from the total columnar aerosol loading or AOD requires the knowledge or assumption about aerosol vertical distribution (Wang and Christopher, 2003). Aerosol profile is controlled by diverse processes, such as convective transport, in-cloud scavenging, particle growth by condensation, biomass burning emission and injection height, boundary layer mixing

45   and more, depending on different sources and aerosol properties (Wang et al., 2006; Kipling et al., 2013; Yang et al., 2013; Kipling et al., 2016). Due to the complexity in these processes and lack of temporal and spatially resolved information, aerosol vertical profile has large uncertainty and diversity in chemical transport models (Wang et al., 2013; Yang et al., 2013; Koffi et al., 2016). Therefore, measuring accurate aerosol vertical distribution is still a challenge but critical in many research areas.

50   Satellite remote sensing techniques are effective methods to monitor the aerosol vertical profile globally. Active satellite remote sensing, especially space-borne lidar such as Cloud-Aerosol Lidar with Orthogonal Polarization (CALIOP) on board with the Cloud-Aerosol Lidar and Infrared Pathfinder Satellite Observation (CALIPSO) platform detects aerosol backscattering extinction profile with fine vertical resolution (Winker et al., 2013). However, the global coverage of CALIOP is less than 0.2% due to its narrow swath and wide gaps between orbits. In contrast, the larger spatial coverage of passive

55   remote sensing measurements overcomes this shortcoming. With the retirement of CALIPSO in August 2023, passive remote sensing will become the only routine technique from space for filling the data gap of measuring aerosol vertical distribution before next lidar dedicated to measure aerosols are launched into space. However, only limited information for aerosol extinction vertical profile can be obtained in passive remote sensing due to the need for multiple assumptions regarding surface and aerosol properties in the retrieval process (Geddes and Bösch, 2015; Rao et al., 2022). Several parameters, including

60   spectral coverage, radiance, polarization, spectral resolution, signal-to-noise ratio (SNR), and the number of viewing angles, can influence the information content and retrieval uncertainties of aerosol profiles. Choi et al. (2021) found that in a single California Laboratory for Atmospheric Remote Sensing Fourier Transform Spectrometer (CLARS-FTS) measurement, the degrees of freedom for signal (DOFS) increase from 2.1 to 2.8, which becomes sufficient for three parameter retrievals (AOD, aerosol peak height, and aerosol layer thickness), when adding high spectral resolution (with a full-width half-maximum of 3

cm-1 or better) and incorporating polarimetric measurements, ensuring a SNR of at least 212, in conjunction with radiance measurements featuring an SNR of 300 for both O2 A and 1Δ bands. Moreover, while satellite instruments, such as TROPOMI and EPIC, lack adequate degrees of freedom for signal (DOFS) on an individual basis, their integration with joint radiometric and polarimetric measurements of the O2 A and B bands—with a resolution of 3 cm-1, a radiance SNR of 500, and a polarization SNR of 353—acquired at three viewing angles, enables the simultaneous retrieval of the three aerosol parameters (Choi et al., 2021).

Hence, instead of retrieving multi-layered aerosol extinction, many algorithms have been developed to derive one piece information of aerosol vertical distribution, aerosol layer height (Aragão et al.)ALH), approximating the altitude of aerosol layer. These passive sensing techniques include stereo photogrammetry, polarimetric techniques in UV-VIS spectrum, IR technique, and atmospheric oxygen (O_2) absorption change Kim et al., 2023) (Pierangelo et al., 2004; Muller et al., 2007; Zeng et al., 2008; Vandenbussche et al., 2013; Wu et al., 2016; Xu et al., 2018; Kim et al., 2023). Not only different physical theories are these techniques based on, but each product has different definitions of ALH and parameterizations of aerosol profiles, including aerosol optical centroid height (AOCH), aerosol effective height (AEH), etc. Part of this study will analyse how the assumption of the shape of aerosol vertical profiles in the retrieval may lead to inherent differences in the retrieval product. Beyond this theoretical analysis, this study mainly focuses on evaluating three ALH data products retrieved from three different satellite sensors that detect the TOA measurements in various O_2 absorption bands from visible to near-infrared: TROPOMI, EPIC/DSCOVR and GEMS.

The light travels longer path when aerosols locate at lower altitude than those at higher altitude, leading to more absorption from more O_2 molecules in longer path (Ding et al., 2016; Xu et al., 2019). As a result, the scattered radiation received by satellite decreases when aerosol layer decreases. Kokhanovsky and Rozanov (2010) retrieved the top height of dust layer by fitting spectral TOA reflectance measurements from O2 A band (close to 760 nm) of the Scanning Imaging Absorption spectroMeter for Atmospheric CHartographY (SCIAMACHY). Moreover, the official operational ALH product of TROPOspheric Monitoring Instrument (TROPOMI) on board the Sentinel-5 Precursor (S5P) mission (hereafter KNMI algorithm) is also retrieved using the O2 A band (Veefkind et al., 2012). However, it is challenging to retrieve ALH over land including both vegetation and soil surfaces from O2 A band since TOA reflectance is dominated by large contributions from high surface reflectance instead of aerosol scattering in this band; as a result, the TOA reflectance is less sensitive to ALH and the uncertainty of surface reflectance leads to large error in ALH retrieval (Xu et al., 2019). Indeed, TROPOMI ALH retrieval from KNMI algorithm over land has higher biases of 2 km (Nanda et al., 2020).

In contrast, although the oxygen absorption is weaker in the O2 B band (close to 688 nm) than in the O2 A band, the surface reflectance is much lower in the O2 B band for all land types and beneficial for aerosols retrieval. Based on this principle, (Xu et al., 2017; Xu et al., 2019) have developed a retrieval algorithm combining O_2 A and B band and applied it on Earth

Polychromatic Imaging Camera (EPIC)/Deep Space Climate Observatory (DSCOVR) observations. An improved algorithm
100   was also developed and applied in hyperspectral measurements from TROPOMI, shorten as O_2AB-UI algorithm hereafter.
Compared with KNMI's product, which shows a bias of 2km over the land, TROPOMI ALH from O_2AB-UI algorithm shows
~0.5 km bias over both ocean and land (Chen et al., 2021b; Nanda et al., 2020). Therefore, in this study, we use TROPOMI
ALH retrieved from a combined use of O2 A and B bands developed by O_2AB-UI rather than KNMI's official operational
product retrieved from single O2 A band.

105

In addition, oxygen-dimer (O_2–O_2) absorption bands are also sensitive to ALH similar to O_2 absorption bands. Aimed to
observe from 300 to 500 nm, the Geostationary Environment Monitoring Spectrometer (GEMS) can measure radiation in
multiple O_2–O_2 absorption bands, such as 340, 360, 380 and 477 nm band, in which 477 nm is found to be the most sensitive
to the ALH due to the largest O_2–O_2 absorption (Chimot et al., 2017; Cho et al., 2023; Kim et al., 2020; Park et al., 2016).
110   GEMS provides an aerosol layer height product (called aerosol effective height, AEH) retrieved from 477 nm O_2–O_2 absorption
band. This algorithm has been applied in OMI measurements, and recently been evaluated with CALIOP, revealing negligible
bias and a standard deviation of 1.4 km in the AEH difference across the GEMS observation domain from January to June
2021 (Park et al., 2023; Park et al., 2016).

115   The three oxygen-related bands, namely, O_2–O_2 477 nm band, O_2 A and B bands, have differences in terms of oxygen
absorption strength and surface reflectance, leading to their diverse sensitivities to ALH and different influences on the ALH
retrievals. Hence, comparing the retrievals from different O_2 absorption bands can help us better understand their different
advantages and disadvantages in ALH retrieval. This motivates us to validate three different satellite ALH products, GEMS,
EPIC and TROPOMI, using CALIOP three-dimensional aerosol extinction product and intercompare among them.
120   Furthermore, the diurnal variation of ALH can be found from hourly GEMS products as a big advantage, but it is a challenge
to validate their accuracy. The close-hourly EPIC global ALH retrievals provide a significant data source for evaluation of the
diurnal variation from GEMS.

Evaluation of ALH retrievals cannot be isolated without providing the retrieval context in which AOD and UVAI are important
125   factors. Accurate retrieval of ALH requires reliable retrieval of AOD, and past studies have shown that ALH and UVAI
relationship can change with AOD (Xu et al., 2017). Hence, AOD and UVAI will also be evaluated. Considering that the
spatial coverage of CALIOP is limited, we carefully selected "gold" cases where dust and smoke events favour the retrievals
from all three sensors. This selection can maximize the signal to noise ratio for ALH retrieval, and hence, the evaluation can
shed light on the future improvement to bring the closure of these three types of retrievals. In addition to pixel-by-pixel
130   comparison of these passive satellite products, they are also assessed with CALIOP aerosol extinction profiles along CALIOP's
track. We provide a detailed comparison with CALIOP profiles for a dust and a smoke plume case. Data and comparison
approach used in this paper are introduced in section 2. The comparison results for all data used in this study are shown in

section 3, while ALH variation during transport for selected dust and smoke case are investigated in section 4. Finally, conclusion and discussion are provided in section 5.

2 Data and methodology

Although the three ALH products compared in this study are all retrieved from oxygen (or its dimer) absorption band, there are still some distinctions about the details in each of three algorithms that may lead to inherent differences in ALH retrievals. However, consistency exists in three algorithms in terms of aerosol vertical profile shape is assumed; all algorithms assume quasi-Gaussian distribution described by two parameters including centroid height and half width (fixed at 1 km) at half maxima. Meanwhile, differences also arise in the definition of ALH. In section 2.1, we first introduce the characteristics of each passive product, together with the details of each retrieval algorithm, and their key differences are highlighted. The difference of ALH definitions is compared in section 2.2. Lastly, the approaches for comparing ALH data and for evaluating them with ground-based observations or active measurements are illustrated in section 2.3.

2.1 Satellite data

2.1.1 GEMS

GEMS offers two products describing aerosol altitude, aerosol effective height (AEH) and ALH, each derived from different algorithms. GEMS ALH product employs an optimal estimation method, incorporating measurements at six wavelengths, including the O2-O2 band at 477 nm (Cho et al., 2023; Kim et al., 2018). In contrast, GEMS AEH algorithm uses the sensitivity of the O2-O2 band similar to the O_2AB-UI algorithm using O2A and B band for TROPOMI and EPIC. Therefore, this study specifically focuses on analyzing AEH version 2.0. Based on the AEH algorithm by Park et al. (2016), a look-up table (LUT) was generated from radiative transfer simulation connecting the O_2-O_2 slant column density (SCD) in 477 nm with AEH for different aerosol types, AOD and surface reflectance. Hence, using the inputs of O2-O2 SCD derived from GEMS observations, as well as the additional information about aerosol types and AOD from GEMS AOD retrievals (Kim et al., 2018) and surface Lambertian equivalent reflectance (LER) climatology, the AEH is derived from the LUT approach. Three aerosol types including highly absorbing fine particles (i.e., smoke), dust and non-absorbing (scattering) aerosols with different optical properties are considered in GEMS aerosol retrieval; aerosol types are classified by the ultraviolet aerosol index (UVAI) and visible aerosol index derived from GEMS observations (Cho et al., 2023). For LUT generation, aerosols are assumed to be spherical and their particle size distribution, refractive index and fine mode fraction for each aerosol types are derived from global AERONET inversion climatology. From a geostationary orbit about 36000 km above the equator, GEMS provides hourly measurements over Asia within the latitudes of 5°S to 45°N and the longitudes of 80°E to 152°E. Given the lower signal-to-noise ratio (SNR) in the morning due to large solar zenith angle (SZA), GEMS only scan the east half of the field of regard, leading to less products available over west region. The total amount of hourly products in each day also depends on the SZA in different seasons. The spatial resolution of GEMS products is 3.5 × 8 km (north-south and east-west) at Seoul, South Korea.

2.1.2 EPIC / DSCOVR

165 Carried on the Deep Space Climate Observatory (DSCOVR) spacecraft at the sun-Earth Lagrange-1 point (L1) 1.5 million km from the Earth, Earth Polychromatic Imaging Camera (EPIC) captures the image for sunlit disk of Earth every 60-100 mins per day. As a result, EPIC monitors the half globe close-hourly, rendering a full disk of 2048×2048 pixels at the spatial resolution of size of 12 km at the Earth surface (Marshak et al., 2018). With 10 narrow channels, EPIC detects the Earth-reflected solar radiance from ultraviolet (Marlier et al.), visible, to near-infrared (NIR) bands, including both O2 A and B

170 bands. The fact that the lower surface reflectance in O2 B band than O2 A band over land (Xu et al., 2019) motives us to use O2 B band to improve the ALH retrievals that use O2 A band only. Xu et al. (2017) developed an algorithm to retrieve aerosol optical central height (AOCH) from EPIC measurements in O2 A and B bands (O$_2$AB-UI algorithm) at the first time and applied it for dust plumes in Atlantic Ocean. Later, Xu et al. (2019) added smoke model in the LUT to improve this algorithm and applied it into several smoke plume cases over the Hudson Bay-Great Lakes area in North America. Based on this

175 algorithm, Lu et al. (2021) updated EPIC level 1 data calibration and analysed the EPIC AOCH for U.S. smoke plumes during 2020 California big wildfires. The validation of EPIC AOCH retrievals with the extinction weighted AOCH from lidar observations (CALIOP) in these papers show high accuracy for absorbing aerosols. In this study, to compare with GEMS observations in East Asia, a new LUT developed for dust plumes in East Asia based on the multi-year AERONET inversion products in this region is added in Lu et al. (2023). The method to select dust inversions from AERONET data follows previous

180 studies (Dubovik et al., 2000; Xu et al., 2017). Furthermore, the UV aerosol index (UVAI) calculation from a method similar to Torres et al. (2007) is implemented in EPIC AOCH retrieval algorithm. Given the reliability of O$_2$AB-UI algorithm for aerosols absorption and AOD, only those pixels covered by lofted layer of absorbing aerosols with UVAI larger than 1.5 and AOD larger than 0.2 (at 680 nm) are analysed. The close-hourly EPIC AOCH product is a good reference to evaluate the diurnal variation of GEMS AEH retrievals.

2.1.3 TROPOMI / S5P

185

The TROPOspheric Monitoring Instrument (TROPOMI) on board the Copernicus Sentinel-5 Precursor satellite was launched in October 2017 to measure solar radiation reflected by Earth from UV to shortwave infrared (SWIR) bands including many trace gases absorption bands and the surface and aerosol information. Flying on a polar satellite, TROPOMI provides global atmospheric components products on a high spatial resolution, 5.5 km × 3.5 km (improved from 7 km × 3.5 km since August

190 2019) once every day. Similar to EPIC, TROPOMI also includes O2 A and B bands to be used for AOCH retrieval. However, the hyperspectral measurements from TROPOMI, unlike the EPIC measurement in narrow channels, prevent us to applying the EPIC AOCH algorithm in TROPOMI L1B data directly. Instead, Chen et al. (2021b) developed an alternative algorithm suitable for TROPOMI data to retrieve AOCH with a few improvements. Besides convolving TROPOMI spectrum with high spectral resolution into multiple narrow channels, several steps for cloud mask and dust/smoke classification are implemented

195 according to the unique channels of TROPOMI compared with EPIC. In this study, as previously highlighted in the

introduction, the TROPOMI AOCH product used is from this O2AB-UI algorithm (Chen et al., 2021b). Moreover, the new LUT developed in EPIC retrievals for Asian dust plumes has been added in the algorithm to be applied for East Asia as well. Applying the operational TROPOMI Level 2 UVAI product (Stein Zweers, 2022), only pixels covered by absorbing aerosols with UVAI larger than 0.5 are retrieved. Overall, even though EPIC and TROPOMI algorithms have differences in cloud mask

200 and aerosol type classification, they use the same LUT and least square method to find optimal AOCH from the ratio in O2 absorption to its nearby continuum band (both O2 A and B). The LUT for smoke aerosols used in both EPIC and TROPOMI is still the same as in Chen et al. (2021b). Less valid retrievals from EPIC and TROPOMI than GEMS are expected due to retrievals only for absorbing aerosols from O2 AB algorithm given their stronger sensitivities than scattering aerosols (Chen et al., 2021a). Here, TROPOMI AOCH-O_2AB retrievals are reported in standard latitude-longitude grid (0.05 ˚ × 0.05 ˚).

205 **2.2 Comparison of ALH Definitions**

GEMS, TROPOMI, and EPIC algorithms all operate under the assumption of a quasi-Gaussian vertical distribution of aerosol extinction described by two parameters: centroid height (H) and half width at half maxima (η) fixed at 1 km. This aerosol extinction profile $\beta(z)$ where z is the altitude with respect to surface can be expressed by a generalized distribution function as specified in Eq. (1):

210

$$\beta(z) = W \frac{\exp(-\sigma_H|z-H|)}{[1+\exp(-\sigma_H|z-H|)]^2} \qquad \textbf{Eq. (1)}$$

where H is the altitude with peak aerosol extinction, W is normalization constant related to the columnar loading, and σ_H is defined as: $\sigma_H = \ln(3+\sqrt{8})/\eta$. However, ALH is a general term to describe the altitude of aerosol layer, while the definition of the retrieved ALH varies by algorithm. EPIC and TROPOMI defined their retrieved ALH as H in Eq. (1) and called AOCH

215 (Chen et al., 2021b; Lu et al., 2023; Lu et al., 2021; Xu et al., 2019; Xu et al., 2017). GEMS defines its ALH retrieval as AEH, the altitude above which the aerosol extinction is the $1/e$ of total columnar AOD, as described in Eq. (2):

$$\frac{\int_0^{AEH} \beta(z)dz}{\int_0^{TOA} \beta(z)dz} = 1 - e^{-1} \qquad \textbf{Eq. (2)}$$

In addition, AOCH retrieved from EPIC and TROPOMI O2AB-UI is relative to geographic (ground) surface, whereas GEMS AEH is relative to sea level. Henceforth, for simplicity and consistency, the term ALH will be used to refer to all aerosol height

220 products used in this study, including GEMS AEH, TROPOMI AOCH, and EPIC AOCH. To validate retrievals from passive remote sensing with lidar data, the extinction weighted heights derived from CALIOP 5 km level 2 aerosol extinction profile product at 532 nm following previous studies are used (Chen et al., 2021b; Lu et al., 2023; Lu et al., 2021; Xu et al., 2019). We define CALIOP AOCH as the extinction-weighted height, as specified in Eq. (3):

$$AOCH_{CALIOP} = \frac{\sum_{i=1}^{n} \beta(z_i)\Delta z_i z_i}{\sum_{i=1}^{n} \beta(z_i)\Delta z_i} \qquad \textbf{Eq. (3)}$$

225 where $\beta_{ext,i}$ represents the 532 nm aerosol extinction coefficient at vertical level i with an altitude of z, while Δz_i denotes the thickness of the vertical layer i.

The comparison of different definitions of ALH for the same aerosol vertical distribution is shown in Fig. 1. In an exampled aerosol extinction profile with EPIC or TROPOMI AOCH at 1.5 km, CALIOP AOCH stands higher at 1.65 km, with GEMS

230 AEH being the highest at 1.87 km (Fig. 1a). The difference between EPIC/TROPOMI and CALIOP AOCH decreases as AOCH increases, ultimately disappears when CALIOP AOCH reaches approximately 4 km and beyond. When CALIOP AOCH is below ~1 km, EPIC/TROPOMI AOCH can be as large as 0.5 km lower than CALIOP. GEMS AEH exhibits a larger difference compared to CALIOP AOCH for higher AOCH, and this difference remains relatively constant at approximately 0.3 km for altitudes above ~3 km. Figure 1c illustrates that the difference between GEMS AEH and EPIC/TROPOMI AOCH

235 can reach around 0.8 km near the surface. However, this difference decreases as AOCH increases, ultimately reaching 0.1 km for altitudes above ~3 km. In our further comparison of ALH, we count for these inherent differences by converting one definition to another to ensure consistency.

240
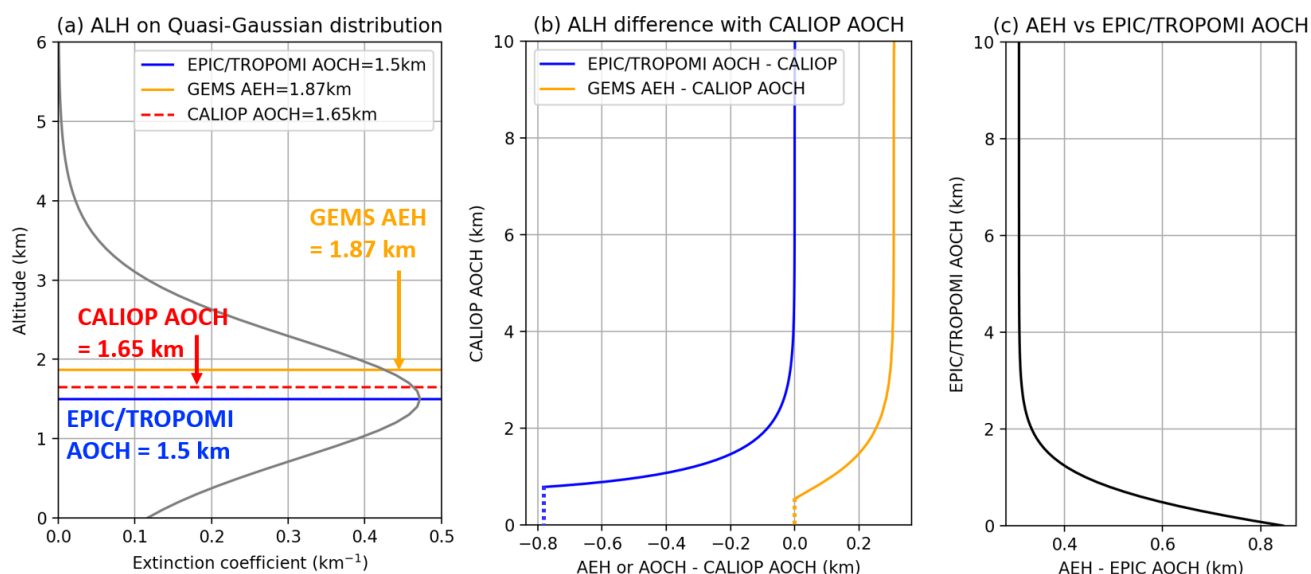
Figure 1. Comparison of ALH definition (GEMS, EPIC, TROPOMI, and CALIOP). (a) Relative heights within the quasi-Gaussian distribution when EPIC/TROPOMI AOCH is 1.5 km. (b) Difference between ALH from passive satellite with CALIOP AOCH. Note that EPIC/TROPOMI AOCH is depicted as dotted vertical lines when it becomes negative below a specific CALIOP AOCH. (c) Difference between GEMS AEH and EPIC/TROPOMI AOCH definitions with respect to the altitude of EPIC/TROPOMI AOCH.

245

2.3 Comparison Approach

Given the availability of EPIC/TROPOMI retrievals for absorbing aerosols, we focus our comparison on a selection of "gold"
dust and smoke cases observed within GEMS field of regard from 2021 to 2023, as listed in Table 1 and corresponding to the
study domain depicted in Fig. 2. Although EPIC products have similar temporal resolution to GEMS, observations over the
250 research domain vary from 3 to 8 per day depending on the solar geometry. Flying on a polar orbit, TROPOMI only observed
the whole globe once each day, but depending on the latitude of each case, TROPOMI ground track may overlapped, which
can lead to the possibility of two TROPOMI observations for some cases. Considering the differences in spatial and temporal
resolutions among these three products, we first resample the GEMS product to TROPOMI and EPIC spatial resolution using
the pixel area weighted method, and then linearly interpolate the GEMS product with time to match the observation time for
255 the paired TROPOMI and EPIC data (Wang et al., 2020).
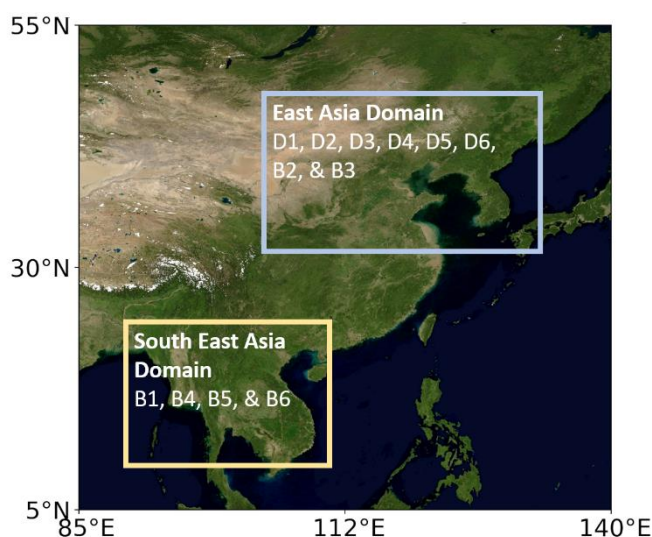
Figure 2. Study domains and cases. "D" represents dust cases, while "B" represents smoke cases ("B" for biomass burning). See Table 1 for more information. Map from Blue Marble: Next Generation from NASA Earth Observatory.

260 **Table 1. Case study dates and the number of observations of each sensor for each domain.**

Case no.	Date	Domain	Number of orbits (or granules)		
			GEMS	TROPOMI	EPIC
D1[a]	2021-03-28	East Asia	7	2	4
D2	2021-04-26	East Asia	8	2	7
D3	2022-04-10	East Asia	8	2	5

D4	2023-03-10	East Asia	7	2	3
D5	2023-05-19	East Asia	8	2	8
D6	2023-05-20	East Asia	8	2	7
B1	2021-03-31	Southeast Asia	6	1	5
B2	2021-08-10	East Asia	8	1	8
B3	2021-08-11	East Asia	6	2	8
B4	2022-04-09	Southeast Asia	8	2	5
B5	2023-03-26	Southeast Asia	6	1	5
B6	2023-04-17	Southeast Asia	8	1	4

[a]: The initial "D" means dust case and "B" represents smoke case from biomass burning.

Since the UVAI product is used in O$_2$AB-UI algorithm to pick up absorbing aerosols, the EPIC and TROPOMI UVAI products are also compared with GEMS since different thresholds might be selected. The ALH comparison and validation for different

265 GEMS UVAI is also conducted to analyze the possible distinction of GEMS ALH retrieval accuracy for different aerosol types. Furthermore, in both O$_2$AB-UI and GEMS algorithm, AOD derived from other window channels is required for retrieving ALH. Hence, the accuracy of each AOD product also influences corresponding ALH retrieval, which will be validated here by the ground-based Aerosol Robotic Network (AERONET) inversions as well. When collocating satellite pixels with ground sites, if the number of valid satellite retrievals is more than 30 % of the total number of pixels within 0.2º

270 radius around AERONET sites, the mean value of those valid satellite AOD retrievals is compared with AERONET AOD. Given satellite overpass time (or observation time for GEMS), AERONET AOD is also averaged between 30 minutes before and after each satellite observation time. In addition, only these satellite data points with a spatial standard deviation less than 0.3 are considered in the comparison for spatial consistency. Since TROPOMI and EPIC AOD products are retrieved at the wavelength of 680 nm whereas GEMS AOD products are retrieved at 354, 443, and, 550 nm, we estimated GEMS AOD at

275 680 nm from its AOD at 443nm by a combined use of aerosol type (dust, smoke, non-absorbing) of each pixel and the Angstrom exponent (440 nm – 677 nm) from GEMS aerosol model for the corresponding aerosol type (Kim et al., 2018). When co-locating passive satellite products with CALIOP pixels along the track, a similar approach to the comparison with AERONET is applied. This involves calculating distance from the center of CALIPSO ground track within a range of 0.2º and adjusting the threshold for valid retrieval to exceed 30 %.

280 **3 Results**

For all the dust and smoke cases in Table 1, the AOD products of GEMS, TROPOMI, and EPIC are first validated against the ground-based AERONET AOD, followed by a pixel-by-pixel intercomparison among the satellite products. Second, the ALH

products from the three passive satellite measurements are validated using the CALIOP level 2 aerosol extinction profile, which are further inter-compared among each other.

3.1 AOD intercomparison and validation with AERONET

The validation of the AOD products from GEMS, TROPOMI, and EPIC against AERONET AOD is shown in Fig. 3. GEMS AOD at 443 nm exhibits a strong positive correlation with AERONET AOD at 440 nm, with correlation coefficients (R) of 0.9 for dust cases and 0.88 for smoke cases (Fig. 3a). The validation results for GEMS AOD at 680 nm for smoke cases indicate a similar statistical agreement (R = 0.84) with 443 nm. In contrast, for dust cases at 680 nm compared with 443 nm, there are notable differences with decreased correlation coefficient (R = 0.73) and a 20 % decrease of RMSE. This indicates possible inaccuracies in the GEMS dust aerosol model but confirms the reliability of the smoke model. GEMS AOD at 680 nm show stronger underestimation than 443 nm, particularly noticeable when AERONET AOD exceeds 0.5. The observed underestimation of GEMS AOD at 680 nm can be in part due to an overestimation of the Angstrom Exponent (AE), which can be affected from inaccurate particle size or refractive index in the wavelength-dependent aerosol model.

For dust cases, both TROPOMI and EPIC AOD exhibit a positive bias compared to AERONET AOD, with values of 0.23 and 0.33 for TROPOMI and EPIC, respectively. Additionally, the comparison between EPIC and TROPOMI AOD with AERONET reveals a slope close to unity for dust cases (EPIC: 0.76, TROPOMI: 1.04), indicating the effectiveness of the dust aerosol model. In contrast to the dust cases, TROPOMI and EPIC AOD exhibit a negligible bias for smoke cases. Furthermore, the lower slope observed in the comparison for smoke cases (EPIC: 0.48, TROPOMI: 0.62) suggests that the smoke aerosol model is not as accurate as the dust aerosol model. The positive y-intercept observed for both EPIC and TROPOMI suggests that the surface reflectance employed in the dust aerosol model may be underestimated, resulting in an overestimation in AOD retrieval. In summary, GEMS consistently underestimates AOD, especially at 680 nm, compared to AERONET AOD. EPIC and TROPOMI, while tending to overestimate AOD in dust cases due to underestimated surface reflectance, show a more accurate dust aerosol model than for smoke.
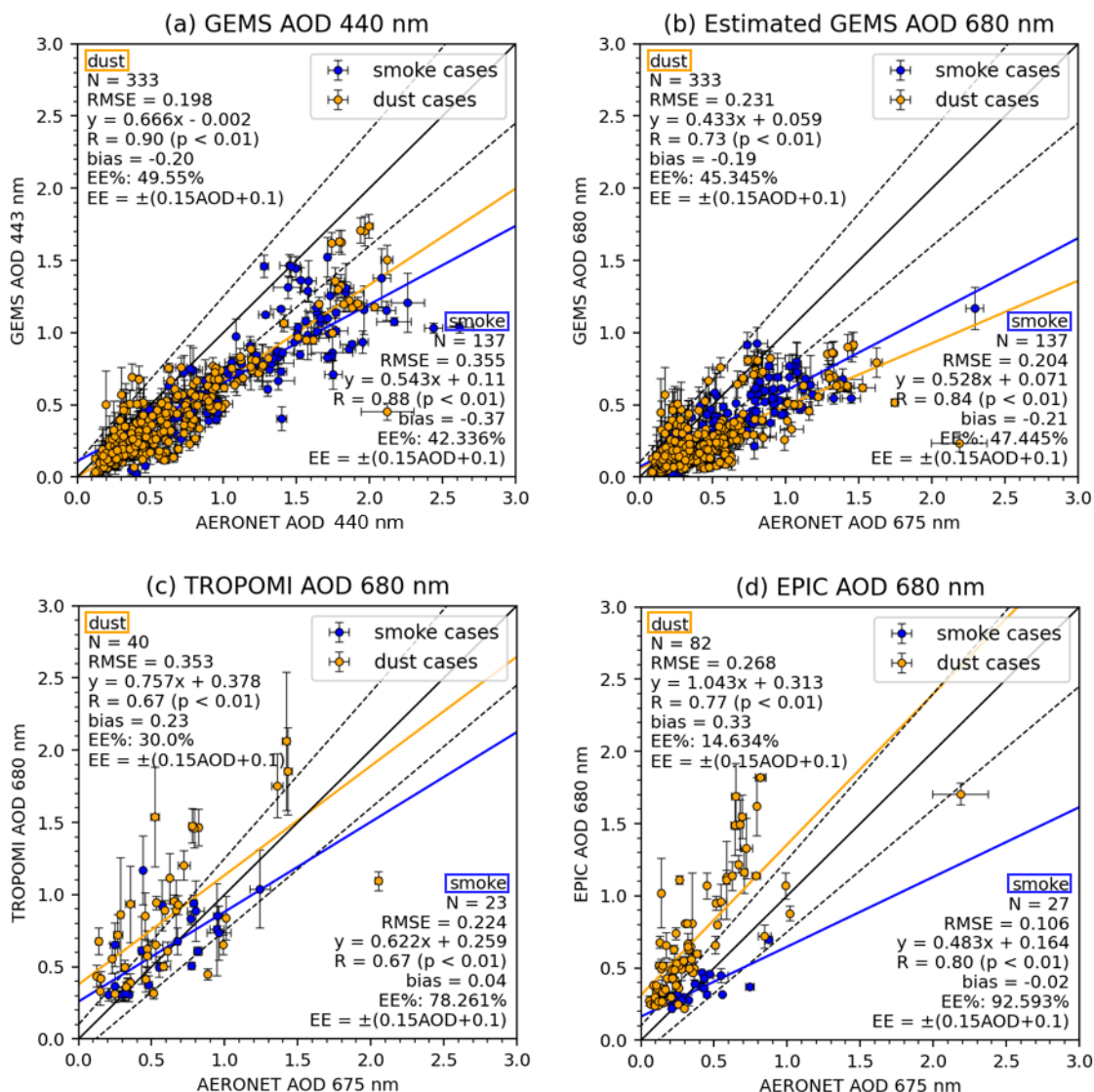
Figure 3. Comparison of GEMS, TROPOMI, and EPIC AOD with AERONET AOD for all cases. The blue and yellow dots denote smoke and dust cases, respectively. (a) Comparison of GEMS AOD at 443 nm with AERONET AOD at 440 nm. Comparison of (b) Estimated GEMS AOD at 680 nm, (c) TROPOMI AOD at 680 nm, and (d) EPIC AOD at 680 nm with AERONET AOD at 675 nm. The solid black line is the 1:1 line, the solid line is the regression line, and the dotted lines are error envelops for AOD (EE = ± (0.15 AOD + 0.1)). Annotated are number of scatter points (N), root mean square error (RMSE), correlation coefficient (R), significance level (p), mean bias, and the percentage of data points within the error envelop (EE). Satellite data points only with a standard deviation less than 0.3 are shown for spatial consistency.

Following the validation with AERONET AOD, Fig. 4 shows the comparison of GEMS AOD with TROPOMI and EPIC AOD, presented separately for dust and smoke cases. For dust cases, GEMS AOD is significantly lower compared with

320 TROPOMI and EPIC, with negative mean biases of -0.44 and -0.53 for EPIC and TROPOMI, respectively. The inaccuracy of the GEMS dust aerosol model, as identified in the previous AERONET validation (Fig. 3), have notable impact on the significant difference of GEMS AOD with TROPOMI and EPIC. Furthermore, the surface reflectance issue observed in TROPOMI and EPIC further contributes to this disparity. The smoke cases show a stronger agreement compared to dust cases, as indicated by decreased negative biases from -0.44 (-0.53) to -0.08 (-0.12) and RMSE values from 0.42 (0.45) to 0.24 (0.17)

325 for TROPOMI (EPIC). The agreement is particularly robust between GEMS and EPIC, as indicated by a high R-value of 0.73. While the smoke aerosol model employed in TROPOMI and EPIC is not as effective as the dust model, its impact on the comparison is relatively minor. These factors on the aerosol model including aerosol properties, fine mode fraction, and the phase function, as well as the single scattering albedo, can largely influence the accuracy of AOD retrievals. A detailed table including the aerosol models employed in the AOD retrieval is provided in the Supplementary (S1).

330
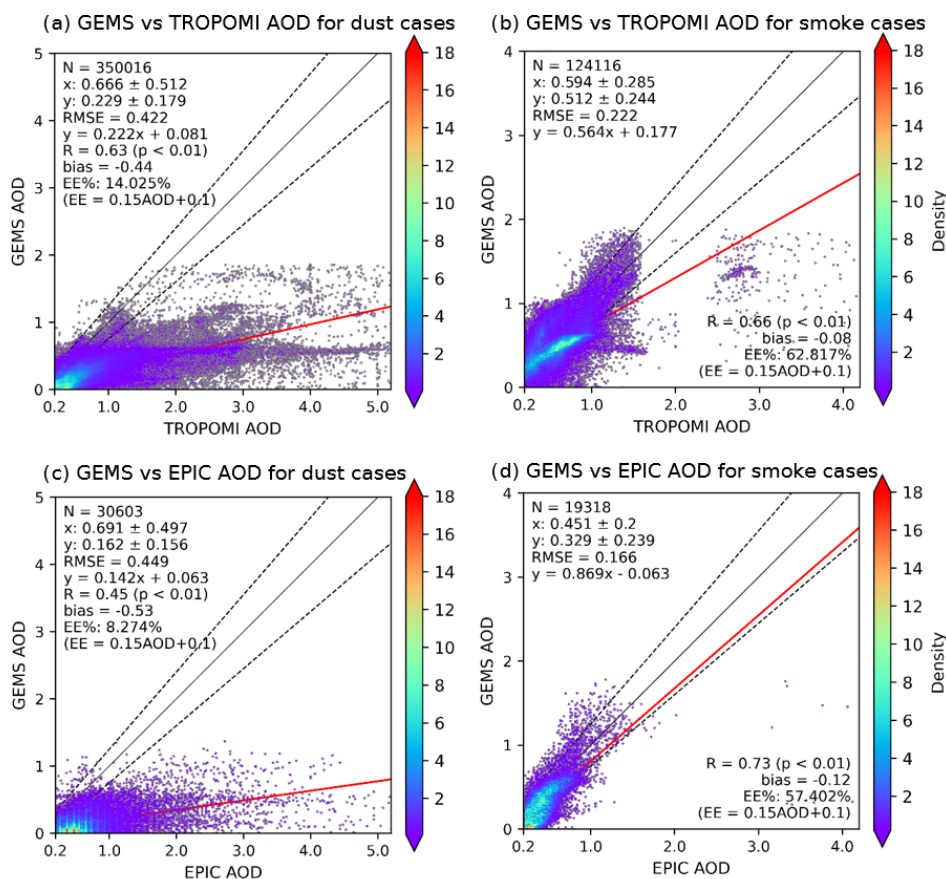
Figure 4. GEMS AOD compared with the corresponding TROPOMI and EPIC products for dust and smoke cases. Scatter density plots of (a) GEMS AOD versus TROPOMI AOD for dust cases, (b) same as (a) but for smoke cases, (c) GEMS AOD versus EPIC AOD for dust cases, and (d) same as (c) but for smoke cases. Black solid line is the one-to-one line, and the red solid line is the regression line. The dotted lines on the AOD comparison plots (a), (c), indicates error envelops (EE = ± 0.15 AOD + 0.1). TROPOMI and EPIC AOD does not have retrieval for less than 0.2, therefore, the figures axis start from where the data exists.

3.2 UVAI intercomparison

The UVAI products of the three satellites are compared, because UVAI is used as a criterion to exclude non-absorbing aerosols for the current TROPOMI and EPIC AOCH retrievals. Figure 5 compares GEMS UVAI with TROPOMI UVAI (Fig. 5a) and EPIC UVAI (Fig. 5b) for all cases. Compared with TROPOMI, GEMS UVAI is systematically higher with a positive mean difference of 1.21. Compared with EPIC, GEMS also exhibits a positive bias, although to a lesser extent (0.32), and shows a higher correlation (R = 0.57). This suggests that when employing UVAI as a filtering criterion for identifying absorbing aerosols in the EPIC and TROPOMI AOCH retrievals, it is important to establish a threshold that takes into account the differences among these distinct products. The differences in the GEMS, TROPOMI, and EPIC UVAI products can be caused by several reasons. First, different wavelengths are used to derive the UVAI product: GEMS UVAI is derived from radiances

at 354 nm and 388 nm, whereas TROPOMI and EPIC UVAIs are derived from radiances at 340 nm and 380 nm. Additionally,

350 different surface altitude and reflectance can cause the differences of their UVAI retrievals. To summarize, GEMS UVAI is

systematically higher than TROPOMI and is more comparable to EPIC.
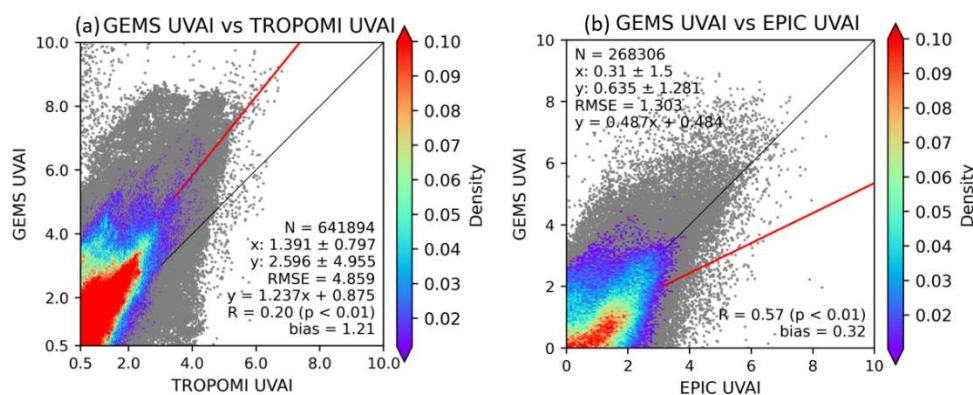
Figure 5. Comparison of GEMS UVAI with corresponding TROPOMI and EPIC products. Scatter density plots illustrating (a)
355 **GEMS UVAI vs. TROPOMI UVAI and (b) GEMS UVAI vs. EPIC UVAI. The one-to-one line is represented by a black solid line,**
while the regression line is shown in red. Dust and smoke cases are combined due to their similarity. Note that TROPOMI UVAI
does not include retrieval values below 0.5, thus the axis begins at a minimum value of 0.5.

3.3 ALH validation with CALIOP

360 To ensure the comparison of the same variable, it is critical to account for differences arising from different ALH definitions

as detailed in Section 2.2. As such, the ALH values of all passive sensors are converted to AOCH following the CALIOP

AOCH definition when validated by CALIOP data. The comparison between the derived AOCH for the three passive sensors

and the CALIOP AOCH is depicted in Fig. 6. Both EPIC and TROPOMI show higher AOCH values compared to CALIOP,

with a bias of 0.8 km for both sensors. Additionally, the RMSE for EPIC and TROPOMI are 1.25 km and 1.31 km, respectively.

365 In contrast, GEMS shows a minimal bias, accompanied by a lower RMSE of 0.75. Despite the overestimation observed in

EPIC and TROPOMI, their correlation with CALIOP is notably high (R=0.75 and R=0.71 respectively), while GEMS exhibits

a slightly lower correlation (R=0.64) The major contribution to the overestimations observed in EPIC and TROPOMI come

from the smoke cases over Southeast Asia (B4, B5, and B6). This suggests a potential issue with the smoke aerosol model in

the EPIC and GEMS AOCH algorithms when applied over Southeast Asia, which warrants further investigation.

370

GEMS retrieves AEH for both absorbing and non-absorbing aerosols, resulting in a larger dataset available for comparison. In

contrast, EPIC and TROPOMI exclusively retrieve ALH for absorbing aerosols, which are determined based on UVAI (e.g.,

UVAI > 1 for TROPOMI and UVAI > 1.5 for EPIC). It is therefore desirable to assess the GEMS AEH retrieval accuracy under different aerosol characteristics. We categorize GEMS aerosol retrievals into two groups using a GEMS UVAI threshold

375 of 3 (UVAI < 3 and UVAI ≥ 3) in the subsequent analyses (Fig. 6c-d). The overall agreement between GEMS and CALIOP is better for aerosols with UVAI ≥ 3 than those with UVAI < 3, particularly for dust cases, as evidenced by a higher R-value (0.75 compared to 0.42) and a lower RMSE (0.33 compared to 0.89). The improved performance for UVAI ≥ 3 can be attributed to the stronger signals of aerosol layers detected in the O2-O2 absorption band. Furthermore, as observed in Fig. 6b, the mean bias of ALH tends to be higher at 0.2 in smoke cases compared to -0.01 in dust cases.

380
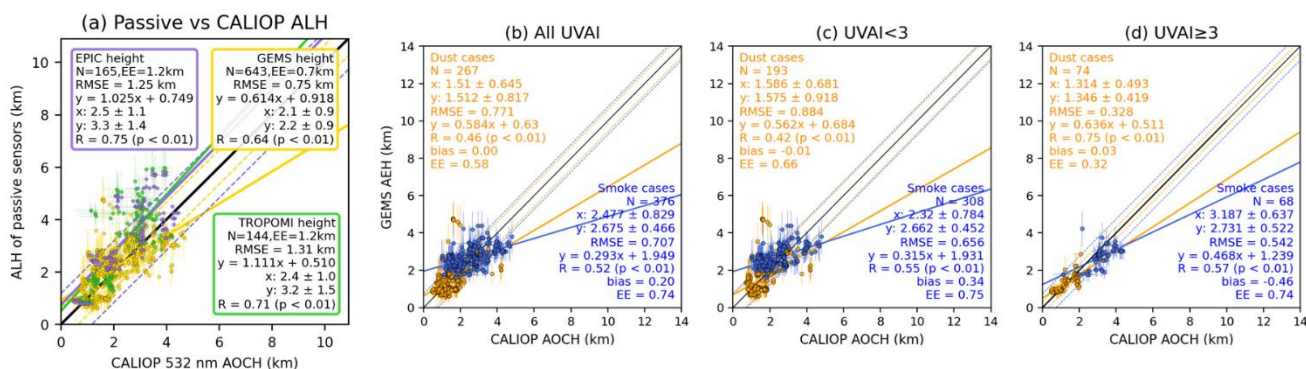
Figure 6. Comparison of GEMS, TROPOMI, and EPIC ALH with CALIOP measurements for all cases. (a) Scatterplot of GEMS (yellow), TROPOMI (green), and EPIC (purple) ALH versus CALIOP AOCH. The black solid line indicates one-to-one line and the dotted lines represent error envelop within which one standard deviation data points are for each passive satellite product. Panels
385 **(b) – (d) are scatter plots of GEMS AEH versus CALIOP AOCH: (b) is for all data points, (c) is ALH comparison for less absorbing aerosols (GEMS UVAI < 3), and (d) is for absorbing aerosols (GEMS UVAI ≥ 3). For (b) – (d), orange dots indicate data points for dust cases and blue dots for smoke cases. Annotated in blue are the statistics for smoke cases, and orange are for dust cases.**

3.4 Passive ALH inter-comparison

390 Upon resampling GEMS products to match the spatial resolution of TROPOMI and EPIC, we synchronize the observation times through linear interpolation of the hourly GEMS products to facilitate a pixel-by-pixel comparison between GEMS ALH and TROPOMI and EPIC ALH. To address the possible discrepancies stemming from different ALH definitions mentioned in Section 2.2, GEMS AEH is converted to align with the EPIC and TROPOMI AOCH definition. Furthermore, we categorize GEMS aerosol retrievals into two groups (UVAI < 3 and UVAI ≥ 3), similar to the analyses in Section 3.3.

395 The results of the ALH inter-comparison for both dust and smoke cases are given in Fig. 7. The GEMS ALH exhibits a narrower range compared to TROPOMI and EPIC, which can be attributed to the different range limits used in their algorithm lookup table (LUT). GEMS only allows ALH to vary within the range from 0.2 to 5 km, while EPIC and TROPOMI use a LUT allowing the ALH to extend from 0 to 9 km (Park et al., 2023). Moreover, GEMS ALH exhibits a negative mean

difference of -0.25 and -0.62 when compared to EPIC and TROPOMI, observed across all dust and smoke cases, and across
400   both UVAI classifications. It is observed that aerosols with UVAI ≥ 3 exhibit a stronger correlation with GEMS AEH compared
with aerosols with UVAI < 3. This can be attributed to the O2 or O2-O2 absorption band being more sensitive to aerosols with
higher UVAI values. Setting the UVAI threshold to 4 enhances the statistical performance for UVAI ≥ 4, with an increase in
correlation coefficients from 0.48 (TROPOMI) and 0.39 (EPIC) to 0.61 (TROPOMI) and 0.46 (EPIC). Detailed results are
provided in the Supplementary (S2).

405
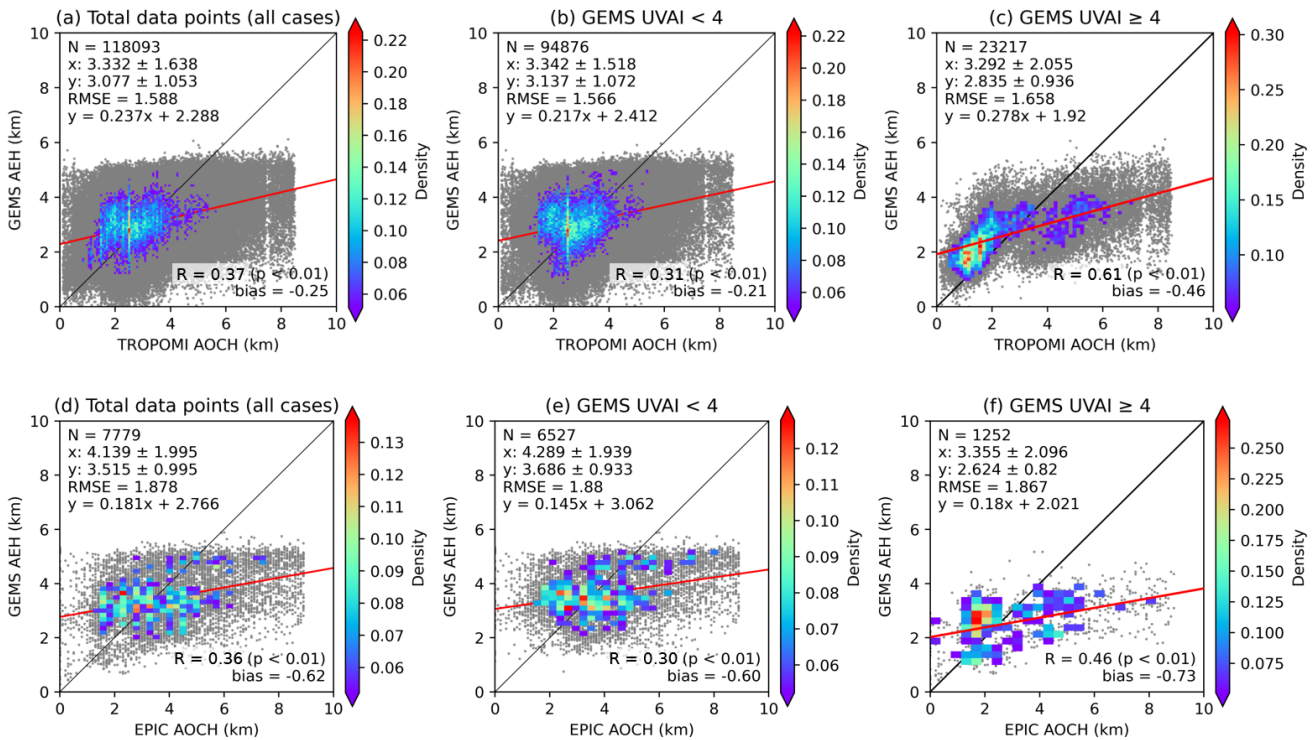
Figure 7. Intercomparison of ALH products from GEMS, TROPOMI and EPIC for dust and smoke cases as a function of UVAI. Density scatter plot of (a) GEMS and TROPOMI ALH comparison and (d) GEMS and EPIC ALH comparison for all dust cases. (b) and (c) are same as (a) but for GEMS UVAI < 3 and UVAI ≥ 3, respectively. (e) and (f) are same as (d) but for GEMS UVAI < 3 and UVAI ≥ 3, respectively. GEMS AEH converted into EPIC (or TROPOMI) AOCH definition.

3.5 Diurnal variation of GEMS and EPIC ALH

We present the comparison of the diurnal variation in GEMS hourly observations with the close-hourly EPIC ALH retrievals, which provide two to six daily observations within our region of interest. Our study domain encompasses a broad geographical

415 area, and the selected cases span from March to August, introducing seasonality changes resulting in significant shifts in the sun's position. Therefore, we define the relative solar local noon time for a given day as the point when the solar zenith angle at a particular location attains its minimum value. With the relative solar local noon time serving as the central reference point, GEMS and EPIC products for the day are adjusted to relative solar local time accordingly. Figure 8 displays the diurnal variation of both GEMS and EPIC ALH within bi-hourly intervals. The colors of the dots represent the percentage of samples.

420 The diurnal variation of EPIC ALH values exhibits a morning rise, starting from ~ 4 km, reaching its peak around local noon (~ 4.5 km), followed by an afternoon decline (4 km). This diurnal variation of EPIC ALH reflects the typical diurnal cycle of

boundary layer development process, featuring a rise and fall throughout the day. Similarly, GEMS ALH also show morning ascending and afternoon descending, but the descending is stronger than EPIC to be as low as 3 km. Furthermore, GEMS ALH is consistently lower than that of EPIC ALH. For aerosols of UVAI > 3, as depicted in Fig. 8b, GEMS ALH demonstrates a

425   stronger morning increase comparable to EPIC. This implies that smoke and dust plumes, primarily consisting of absorbing aerosols with higher UVAI values, tend to adhere to the boundary layer dynamics consistently throughout the day.
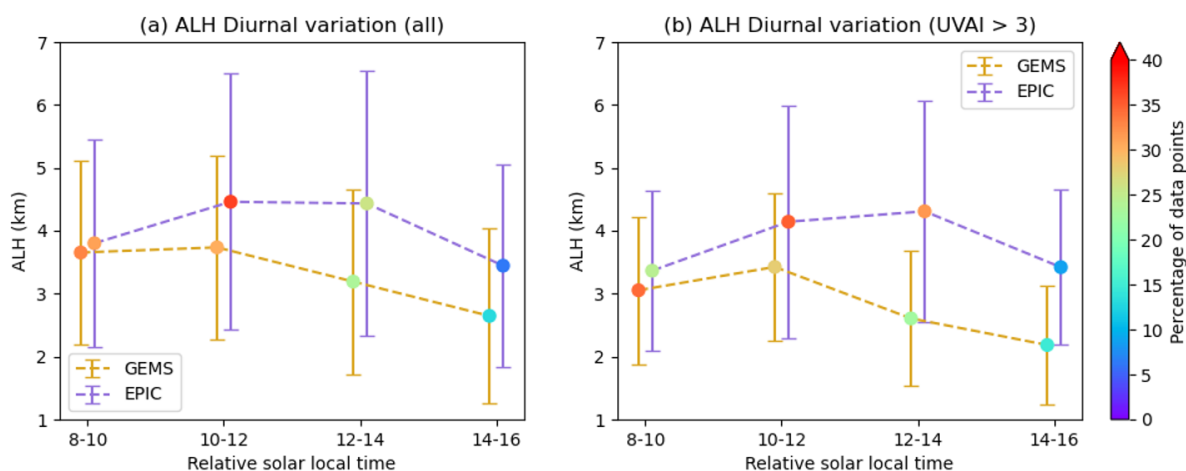
Figure 8. Diurnal variation of ALH between GEMS and EPIC at relative solar local times of 8:00 – 10:00, 10:00 – 12:00, 12:00 –
430   **14:00, and 14:00 - 16:00. (a) ALH diurnal variation for all pixels, (a) same as (a), but only for UVAI > 3. Yellow lines indicate GEMS error bar (standard deviation), purple indicates the corresponding of EPIC, dots represent the number of data points during each time frame. GEMS AEH has been adjusted to match the EPIC AOCH definition.**

4 Case study

We present detailed analysis of GEMS, EPIC, and TROPOMI ALH retrievals during transport for a dust (D1) and a smoke
435   plume (B6). In particular, the diurnal variation of ALH from GEMS and EPIC for the dust or smoke plumes is also discussed.

4.1 Dust plume case

Figure 9 shows GEMS, TROPOMI and EPIC ALH retrievals for a selected dust case on March 28, 2021 (D1). The first row presents GEMS ALH, with magenta lines depicting CALIOP ground track over the GEMS map at the closest time of CALIOP measurement and the second row shows EPIC and TROPOMI ALH aligned with the closest GEMS measurement time. GEMS
440   AEH was adjusted to EPIC/TROPOMI AOCH definition for consistent comparison. The AOD, UVAI products for all satellites are shown in the Supplementary (S3). This case is a spring dust event, originating from the Gobi Desert a few days before it reached over China on 28 March 2021, specifically near Beijing, indicated by the black star on the middle of the research domain (Fig. 9a). In the dust plume area, GEMS ALH peaks at high values (~3 km) at 01:45 and 02:45 (Fig. 9a-b) before

gradually decreasing to ~1.5 km by 06:45 (Fig. 9f). In contrast, EPIC and TROPOMI ALH maintain relatively consistent

445 values at 1~2 km. Likely, multiple GEMS observations reveal clear hourly variations, whereas discerning diurnal changes is

challenging with TROPOMI and EPIC.
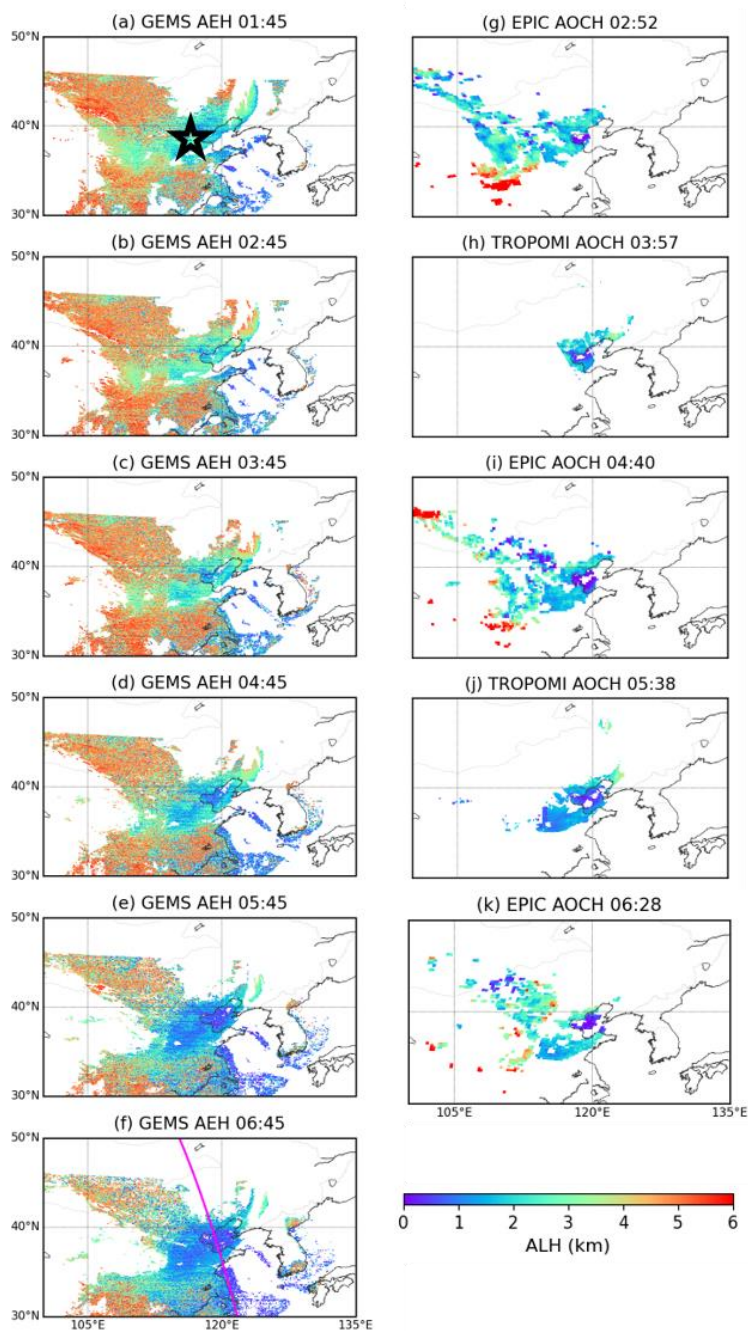
Figure 9. First column (a – f) shows hourly GEMS ALH products presented in timely order from (a) 01:45 to (f) 06:45 (UTC). Second column (g – k) EPIC and TROPOMI ALH aligned with the nearest time of GEMS measurement time for a dust plume case on 28 March 2021. CALIOP ground tracks are shown as the magenta line on the GEMS ALH map (first column) where it has the closest observation time with GEMS.

Comparison of GEMS, TROPOMI, and EPIC ALH with CALIOP ALH for this dust case is shown in Fig. 10. GEMS has the
455   greatest number of data points due to its valid retrievals for both scattering and absorbing aerosols and its high spatial
resolution. For this specific case, EPIC ALH show the highest correlation coefficient among all (R = 0.74) and TROPOMI
ALH also has a high correlation coefficient (R = 0.6) and the lowest RMSE of 0.33 km. Although CALIOP can capture multiple
layers of aerosols from extinction coefficients, passive sensors used in this study assume single aerosol layer, thereby retrieving
ALH where stronger signal is detected. In Fig. 10b, CALIOP identifies two aerosol layers with a discontinuous extinction
460   coefficient at 38º N latitude and 119.5º E longitude. In contrast, passive sensors like GEMS and TROPOMI exhibit continuous
retrievals, consistently following the stronger signal. Consequently, discrepancies between CALIOP and passive sensors may
be more pronounced in the presence of multiple aerosol layers. Further investigation is needed for a comprehensive study of
multi-layered aerosol plumes.
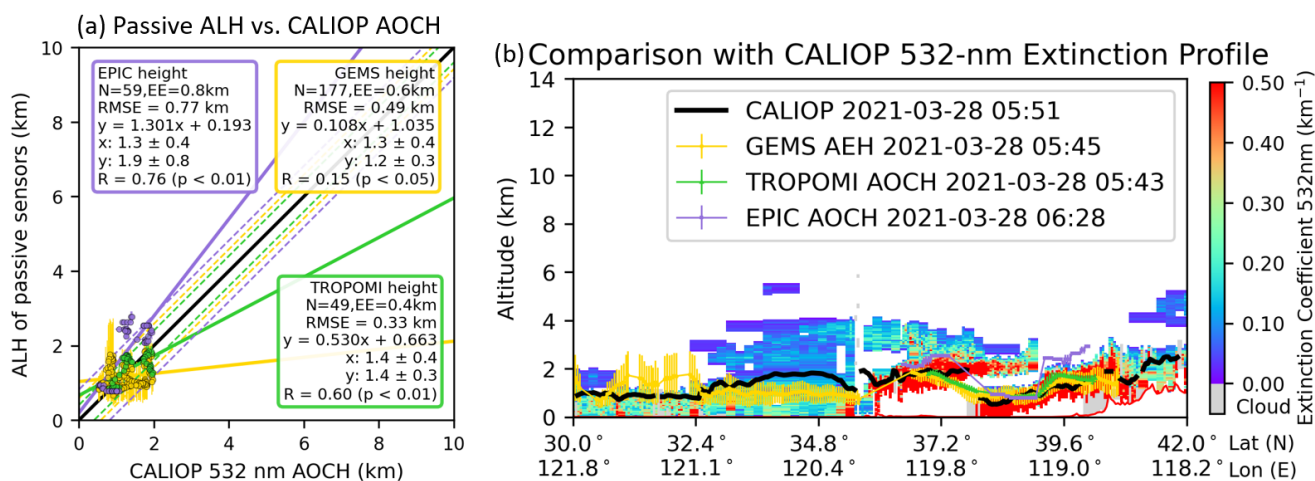
465

**Figure 10. Comparison of GEMS, TROPOMI and EPIC ALH with CALIOP extinction weighted heights for a dust case over East
Asia on 28 March 2021. (a) GEMS, TROPOMI, and EPIC ALH on the vertical profile of CALIOP aerosol extinction curtain plot.
(b) Scatterplot of GEMS (yellow), TROPOMI (green), and EPIC (purple) ALH versus CALIOP AOCH. All converted into CALIOP
AOCH definition.**

470

Figure 11 shows the regional averaged ALH during this dust plume transport from 27 to 29 March 2021. To focus on the
consistent area covered by the thickest dust plume, different UVAI thresholds were empirically selected. Pixels where UVAI
values of their own products are higher than 3, 1, and 2 were considered for GEMS, TROPOMI, and EPIC, respectively. For
CALIOP, collocated pixels along the track with GEMS UVAI > 3 were considered. Maps of regional ALH and UVAI for all
475   products are provided in the Supplementary (S4). The mean ALH values of the dust plume from all products show good
agreement, falling within reasonable error range of < 1 km. From GEMS measurements, the dust plume locates at 4-5 km on
27th March, then descends to ~3 km during 28th March and keeps until 29th, similar as EPIC and TROPOMI measurements,
indicating the deposition process of dust aerosols during transport. Since the number of GEMS measurement reach from 6 to

10 a day, GEMS ALH could catch the dust plume diurnal variation during transport, compensating for the lack of
480   measurements from other satellite platforms (CALIOP, TROPOMI, EPIC).
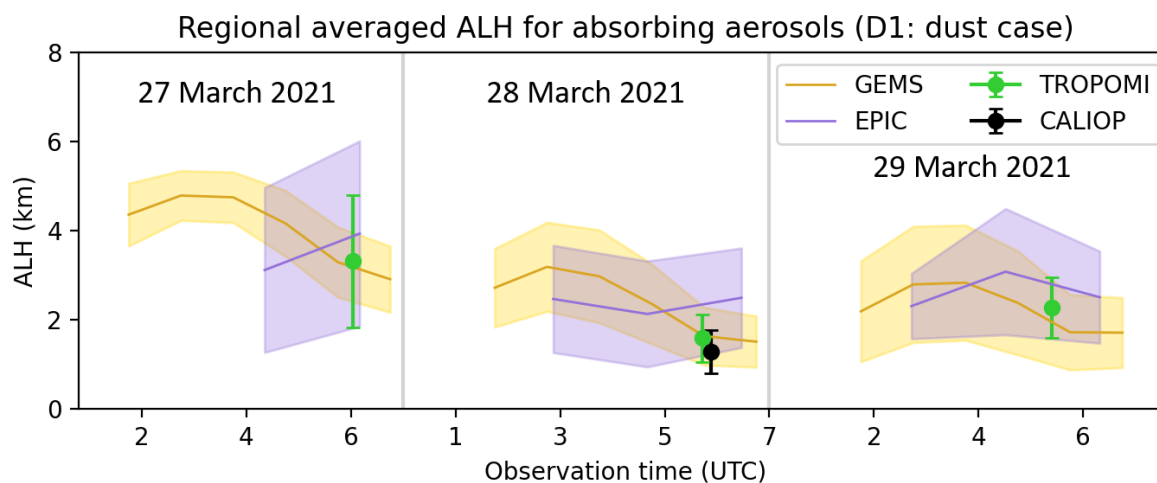
Figure 11. Time series plot of regional averaged ALH for absorbing aerosol for a dust case (28 March 2021). ALH of GEMS, TROPOMI, and EPIC is represented as yellow, green, and purple, respectively. The lines and shadows indicate the mean and the
485   **standard deviation, respectively. CALIOP ALH is represented by black error bar. GEMS AEH, EPIC AOCH, and TROPOMI AOCH are converted to CALIOP AOCH definition.**

4.2 Smoke plume case

Figure 12 displays ALH retrievals from GEMS with TROPOMI and EPIC for one of the selected smoke case on April 17,
490   2023 (B6). The first row displays GEMS ALH and the second row shows EPIC and TROPOMI ALH aligned with the closest
GEMS measurement time. The second row features EPIC and TROPOMI ALH data, aligned with the closest GEMS
measurement time. In addition, AOD and UVAI maps are provided in the Supplementary (S5). GEMS AEH was adjusted for
consistent comparison with EPIC/TROPOMI AOCH. This particular case is a smoke event in Southeast Asia, with the
identified smoke plume situated predominantly over the northern areas of Laos and Thailand, shown in the central part of the
495   domain (20º N, 100º E) indicated by the black star on Fig. 12a. Over the previous decades, the air quality in Southeast Asia
has been periodically affected by the transboundary smoke and haze issue, primarily linked to slash-and-burn agriculture and
land clearing practices, particularly during the dry season (Chang and Song, 2010; Shi et al., 2014). GEMS ALH, which
retrieves both absorbing and non-absorbing aerosols, has broader coverage compared to EPIC/TROPOMI, which exclusively
retrieves absorbing aerosols. Focusing solely on the smoke plume, GEMS ALH ranges from 3 to 5 km, while EPIC and
500   TROPOMI consistently show ALH values predominantly exceeding 4 km in land pixels.
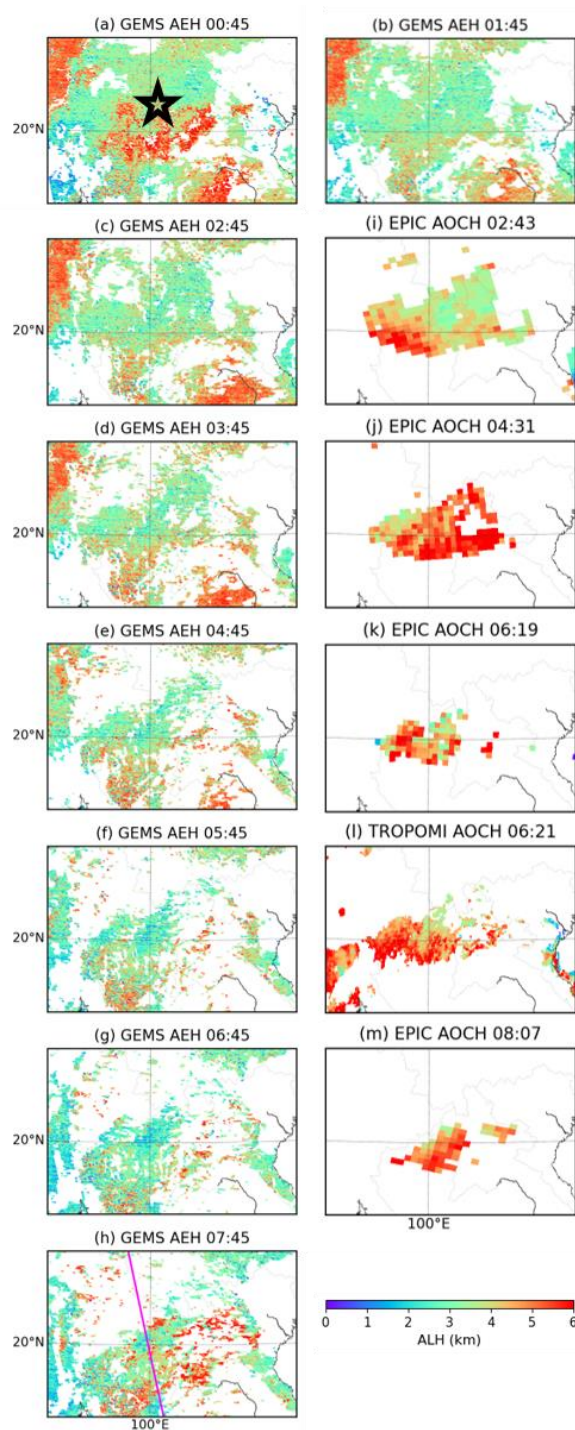
Figure 12. First row (a – f) shows hourly GEMS AEH products presented in timely order from (a) 00:45 to (f) 07:45 (UTC). Second row (g – i) EPIC and TROPOMI AOCH aligned on the nearest times of GEMS measurement time for a smoke plume case on 17 April 2023. CALIOP ground tracks are shown in magenta lines on the GEMS ALH map of the closest time.

Figure 13 presents a comparison with CALIOP ALH, specifically highlighting the northern regions of Laos and Thailand where the smoke plume is detected along the CALIOP ground track. In Fig. 13 and Fig. 14, GEMS AEH and EPIC/TROPOMI AOCH values have been converted to the CALIOP AOCH definition. GEMS and CALIOP ALH show comparability within
510   the range of 2-4 km, as evidenced by a smaller RMSE of 0.75 km. On the contrary, EPIC and TROPOMI ALH values are approximately 2 km higher than CALIOP ALH, yet they display similar vertical distribution patterns of the smoke plume over the region of 19-20° N. This suggests that EPIC and TROPOMI ALH retrievals exhibit a systematic positive bias for aerosols over Southeast Asia, indicating the potential need for tuning in the related smoke model, including surface reflectance and aerosol properties. In general, GEMS ALH demonstrates comparability with CALIOP ALH, whereas both EPIC and
515   TROPOMI ALH tend to overestimate.
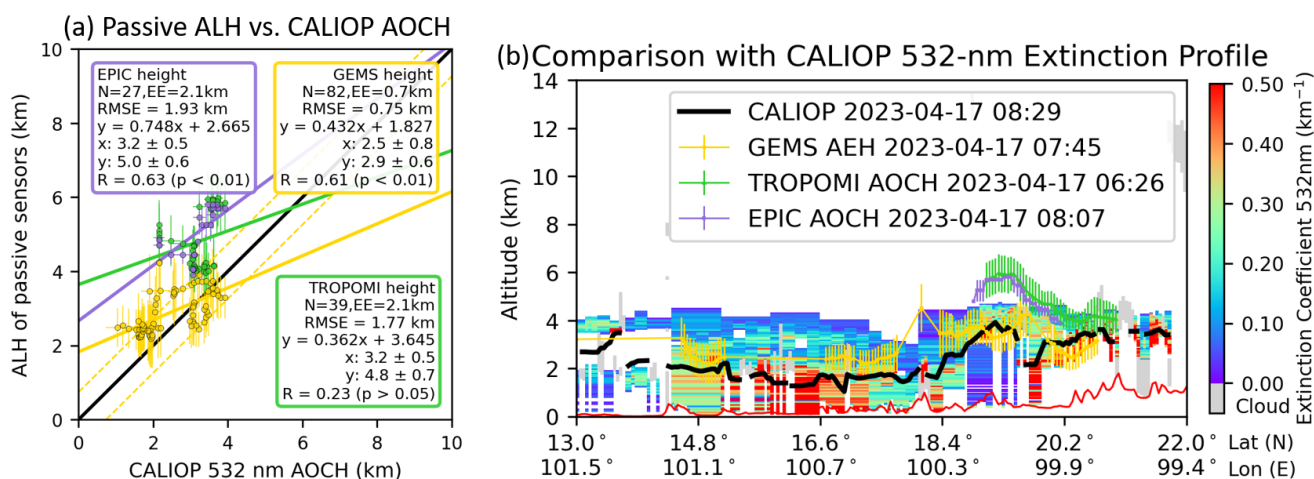
Figure 13. Same as Figure 11 but for a smoke case over Southeast Asia on 17 April 2023.

520   In Fig. 14, we present the regional averaged ALH for absorbing aerosols for this smoke case. UVAI thresholds are chosen to facilitate the comparison of ALH among GEMS, EPIC, and TROPOMI, ensuring a consistent focus on regions with comparable coverage of absorbing aerosols. UVAI thresholds for GEMS, TROPOMI, and EPIC, are set as 3, 1.5, and 2, respectively. Detailed regional ALH map from all products are provided in the Supplemenstary (S6). Notably, since the CALIOP product is included, all GEMS AEH and EPIC/TROPOMI AOCH values have been converted to the CALIOP AOCH
525   definition. In contrast to the dust case discussed in Section 4.1, this smoke plume shows little diurnal variation throughout the day. Post 5 UTC time, GEMS and EPIC exhibit similar patterns, yet EPIC consistently registers ALH values approximately 2 km higher throughout the day. While the observation times of CALIOP do not align with the consecutive data of GEMS, the

regional average of CALIOP ALH falls within the range of GEMS ALH. Additionally, the regional mean of TROPOMI ALH is higher than that of GEMS but lower than EPIC for this smoke plume.

530
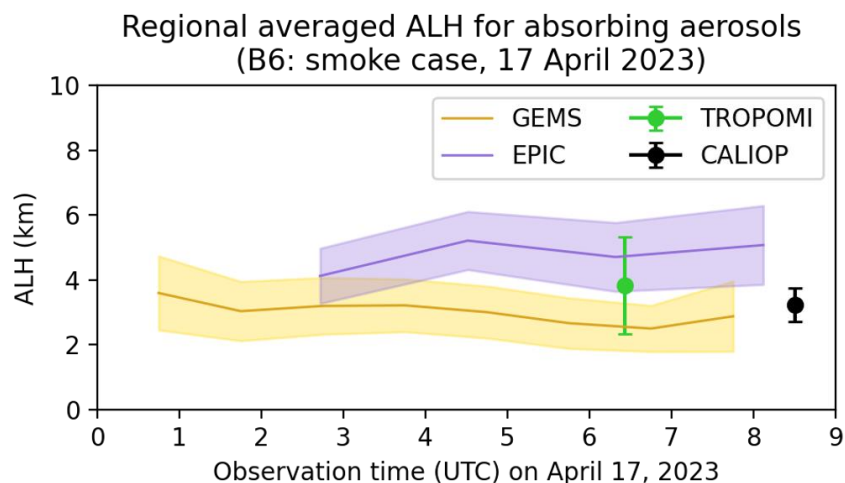
Figure 14. Time series plot of regional averaged ALH for absorbing aerosol for a smoke case (17 April 2023). ALH of GEMS, TROPOMI, and EPIC is represented as yellow, green, and purple, respectively. The lines and shadows indicate the mean and the standard deviation, respectively. CALIOP ALH is represented by black error bar. GEMS AEH, EPIC AOCH, and TROPOMI AOCH are converted to CALIOP AOCH definition.

5 Conclusion and discussion

Aerosol vertical distribution is important for assessing aerosol climate impact, surface air quality, and remote sensing of aerosols. In this study, we compared multiple aerosol layer height products from satellite platforms of GEMS, EPIC, and TROPOMI that use oxygen (or oxygen dimer) absorption bands, specifically O2-O2 band for GEMS, and O2-A and B bands for TROPOMI and EPIC. Several dust and smoke plume cases over different regions in Asia covered by the field of regard of GEMS were selected for comparison. Adjustments have been made to account for the inherent variations in the definitions of aerosol layer height among different products, ensuring an apple-to-apple comparison.

As part of the ALH retrieval evaluation, we also evaluated the AOD retrievals from GEMS, EPIC and TROPOMI with AERONET AOD and compared the UVAI among these satellite platforms. Compared with AERONET, GEMS AOD at 443 nm demonstrates a strong positive correlation in both dust (R = 0.9) and smoke cases (R = 0.88). Discrepancies arise at 680 nm for dust cases, indicating potential inaccuracies in GEMS dust aerosol model. TROPOMI and EPIC tend to overestimate AOD in dust cases due to underestimated surface reflectance. The inaccuracies in the GEMS dust aerosol model significantly contribute to the substantial differences in GEMS AOD compared to TROPOMI and EPIC, further compounded by inaccurate

surface reflectance in TROPOMI and EPIC. In addition, GEMS UVAI is consistently larger than TROPOMI UVAI, by 1.2, whereas it shows a better agreement with EPIC UVAI with a smaller bias of 0.32.

Both EPIC and TROPOMI consistently overestimates ALH in comparison to CALIOP, with an approximate bias of 0.8 km.
555   In contrast, GEMS ALH demonstrated minimal bias but exhibited a slightly lower correlation coefficient (R = 0.64). Categorizing GEMS aerosol retrievals based on a UVAI threshold of 3 revealed better overall agreement with CALIOP ALH for aerosols with UVAI ≥ 3. While comparing GEMS with EPIC and TROPOMI, a narrower range in GEMS AEH was seen due in part to limitations in its algorithm lookup table (LUT) within the range of 0.2 to 5 km, while EPIC and TROPOMI had LUTs extending from 0 to 9 km.

560

EPIC ALH showed a characteristic diurnal cycle aligning with conventional boundary layer development, whereas GEMS ALH values showed minimal morning variation and a subsequent afternoon decrease. Notably, for smoke and dust plumes, predominantly composed of absorbing aerosols with UVAI values exceeding 3, consistently follow the dynamics of the boundary layer throughout the day.

565

Lastly, we presented a detailed analysis on both a dust case and a smoke case to compare differences in spatial and vertical distribution of ALH products, along with diurnal variations. EPIC and TROPOMI ALH show a strong correlation with CALIOP for both the discussed dust and smoke events; however, they tend to overestimate in the smoke case. In contrast, while GEMS ALH has a lower correlation, it consistently shows a smaller mean bias. Additionally, hourly GEMS ALH have
570   the power to catch the diurnal variation of aerosol plumes during transport, compensating for the lack of measurements from other satellite platforms.

In conclusion, our comprehensive analysis provides a thorough evaluation of the performance and comparative assessment of ALH, AOD, and UVAI retrievals from GEMS, EPIC, and TROPOMI. The comparison of the ALH definition among different
575   sensors highlights the need for standardization, ensuring a consistent basis for comparisons. Results from this study help enhance our understanding of aerosol plume characteristics, overcoming challenges associated with previously difficult aspects such as the comparison of ALH diurnal variations. Furthermore, we offer insights for future ALH product development by identifying and addressing the limitations in inputs from each retrieval algorithm, such as the impact of aerosol models and surface reflectance.

580

Code availability

Aerosol layer height and aerosol optical depth analysis codes are available at https://doi.org/10.5281/zenodo.10408292.

Data availability

TROPOMI AOCH with UIowa's AOCH-O2AB algorithm dataset used in this study can be found at
585 http://doi.org/10.5281/zenodo.10407271. EPIC level 2 AOCH data (from UIowa's AOCH-O2AB algorithm) can be found at https://opendap.larc.nasa.gov/opendap/DSCOVR/EPIC/L2_AOCH_01/contents.html. GEMS L2 AEH V2.0 and AERAOD V2.0 can be downloaded from the Environmental Satellite Center website (https://nesc.nier.go.kr/en/html/datasvc/index.do). CALIOP level 2 data are from https://asdc.larc.nasa.gov/data/. Earthdata registration is required for the access to the CALIOP level 2 data.

590 **Author contribution**

HK performed data curation, formal analysis, visualization, and writing most of the original draft. XC was responsible for conceptualization, formal analysis, methodology, writing parts of the original draft, and supervision. XC also provided TROPOMI AOCH data and ZL provided the EPIC AOCH data. JW provided comments on the research design and supervision. MZ contributed on formal analysis and GRC provided comments on writing focus and structure. SSP provided
595 GEMS AEH V2.0 data. All authors including JK provided comments and edited the manuscript.

Competing interests

Jun Wang is a member of the editorial board of *Atmospheric Measurement Techniques*.

Acknowledgements

This was supported by NASA EPIC/DSCOVR Science team program (80NSSC22K0503) and NOAA
600 (1305M322PNRMT0542, 1305M323PNRMN0450, NA23OAR4310303). We thank the National Institute of Environmental Research of South Korea for providing GEMS satellite data. We acknowledge the public availability of CALIOP Level 2 aerosol profile data from the NASA Langley Research Center Atmospheric Science Data Center. We thank all Principal Investigators, Co-Principal Investigators and their staff for establishing and maintaining the AERONET sites used in this investigation.

605

References

Aragão, L. E. O. C., Anderson, L. O., Fonseca, M. G., Rosan, T. M., Vedovato, L. B., Wagner, F. H., Silva, C. V. J., Silva Junior, C. H. L., Arai, E., Aguiar, A. P., Barlow, J., Berenguer, E., Deeter, M. N., Domingues, L. G., Gatti, L., Gloor, M., Malhi, Y., Marengo, J. A., Miller, J. B., Phillips, O. L., and Saatchi, S.: 21st Century drought-related fires counteract the decline of Amazon deforestation carbon emissions, Nature Communications, 9, 536, https://doi.org/10.1038/s41467-017-02771-y, 2018.

Babu, S. S., Moorthy, K. K., Manchanda, R. K., Sinha, P. R., Satheesh, S. K., Vajja, D. P., Srinivasan, S., and Kumar, V. H. A.: Free tropospheric black carbon aerosol measurements using high altitude balloon: Do BC layers build "their own homes" up in the atmosphere?, Geophys Res Lett, 38, https://doi.org/10.1029/2011gl046654, 2011.

Chen, X., Xu, X. G., Wang, J., and Diner, D. J.: Can multi-angular polarimetric measurements in the oxygen-A and B bands improve the retrieval of aerosol vertical distribution?, J Quant Spectrosc Ra, 270, https://doi.org/10.1016/j.jqsrt.2021.107679, 2021a.

Chen, X., Wang, J., Xu, X. G., Zhou, M., Zhang, H. X., Garcia, L. C., Colarco, P. R., Janz, S. J., Yorks, J., McGill, M., Reid, J. S., de Graaf, M., and Kondragunta, S.: First retrieval of absorbing aerosol height over dark target using TROPOMI oxygen B band: Algorithm development and application for surface particulate matter estimates, Remote Sensing of Environment, 265, 18, https://doi.org/10.1016/j.rse.2021.112674, 2021b.

Chimot, J., Veefkind, J. P., Vlemmix, T., de Haan, J. F., Amiridis, V., Proestakis, E., Marinou, E., and Levelt, P. F.: An exploratory study on the aerosol height retrieval from OMI measurements of the 477 nm O-2-O-2 spectral band using a neural network approach, Atmos Meas Tech, 10, 783-809, https://doi.org/10.5194/amt-10-783-2017, 2017.

Cho, Y., Kim, J., Go, S., Kim, M., Lee, S., Kim, M., Chong, H., Lee, W. J., Lee, D. W., Torres, O., and Park, S. S.: First Atmospheric Aerosol Monitoring Results from Geostationary Environment Monitoring Spectrometer (GEMS) over Asia[preprint], https://doi.org/10.5194/amt-2023-221, 23 October 2023.

Choi, M., Sander, S. P., Spurr, R. J. D., Pongetti, T. J., van Harten, G., Drouin, B. J., Diner, D. J., Crisp, D., Eldering, A., Kalashnikova, O. V., Jiang, J. H., Hyon, J. J., and Fu, D. J.: Aerosol profiling using radiometric and polarimetric spectral measurements in the O_2 near infrared bands: Estimation of information content and measurement uncertainties, Remote Sensing of Environment, 253, 20, https://doi.org/10.1016/j.rse.2020.112179, 2021.

Christian, K., Wang, J., Ge, C., Peterson, D., Hyer, E., Yorks, J., and McGill, M.: Radiative Forcing and Stratospheric Warming of Pyrocumulonimbus smoke Aerosols: First Modeling Results With Multisensor (EPIC, CALIPSO, AND CATS) Views from Space, Geophys Res Lett, 46, 10061-10071, https://doi.org/10.1029/2019gl082360, 2019.

Ding, S. G., Wang, J., and Xu, X. G.: Polarimetric remote sensing in oxygen A and B bands: sensitivity study and information content analysis for vertical profile of aerosols, Atmos Meas Tech, 9, 2077-2092, https://doi.org/10.5194/amt-9-2077-2016, 2016.

Dubovik, O., Smirnov, A., Holben, B. N., King, M. D., Kaufman, Y. J., Eck, T. F., and Slutsker, I.: Accuracy assessments of aerosol optical properties retrieved from Aerosol Robotic Network (AERONET) Sun and sky radiance measurements, J Geophys Res-Atmos, 105, 9791-9806, https://doi.org/10.1029/2000jd900040, 2000.

Geddes, A. and Bösch, H.: Tropospheric aerosol profile information from high-resolution oxygen A-band measurements from space, Atmos Meas Tech, 8, 859-874, https://doi.org/10.5194/amt-8-859-2015, 2015.

Kim, J., Jeong, U., Ahn, M. H., Kim, J. H., Park, R. J., Lee, H., Song, C. H., Choi, Y. S., Lee, K. H., Yoo, J. M., Jeong, M. J., Park, S. K., Lee, K. M., Song, C. K., Kim, S. W., Kim, Y. J., Kim, S. W., Kim, M., Go, S., Liu, X., Chance, K., Chan Miller, C., Al-Saadi, J., Veihelmann, B., Bhartia, P. K., Torres, O., Abad, G. G., Haffner, D. P., Ko, D. H., Lee, S. H., Woo, J. H., Chong, H., Park, S. S., Nicks, D., Choi, W. J., Moon, K. J., Cho, A., Yoon, J., Kim, S. K., Hong, H., Lee, K., Lee, H., Lee, S., Choi, M., Veefkind, P., Levelt, P. F., Edwards, D. P., Kang, M., Eo, M., Bak, J., Baek, K., Kwon, H. A., Yang, J., Park, J., Han, K. M., Kim, B. R., Shin, H. W., Choi, H., Lee, E., Chong, J., Cha, Y., Koo, J. H., Irie, H., Hayashida, S., Kasai, Y., Kanaya, Y., Liu, C., Lin, J., Crawford, J. H., Carmichael, G. R., Newchurch, M. J., Lefer, B. L., Herman, J. R., Swap, R. J., Lau, A. K. H., Kurosu, T. P., Jaross, G., Ahlers, B., Dobber, M., McElroy, C. T., and Choi, Y.: New Era of Air Quality Monitoring from Space: Geostationary Environment Monitoring Spectrometer (GEMS), B Am Meteorol Soc, 101, E1-E22, https://doi.org/10.1175/bams-d-18-0013.1, 2020.

Kim, M., Kim, J., Lim, H., Lee, S., Cho, Y., Yeo, H., and Kim, S. W.: Exploring geometrical stereoscopic aerosol top height retrieval from geostationary satellite imagery in East Asia, Atmos Meas Tech, 16, 2673-2690, https://doi.org/10.5194/amt-16-2673-2023, 2023.

Kim, M., Kim, J., Torres, O., Ahn, C., Kim, W., Jeong, U., Go, S., Liu, X., Moon, K. J., and Kim, D. R.: Optimal Estimation-Based Algorithm to Retrieve Aerosol Optical Properties for GEMS Measurements over Asia, Remote Sens-Basel, 10, https://doi.org/10.3390/rs10020162, 2018.

655 Kipling, Z., Stier, P., Schwarz, J. P., Perring, A. E., Spackman, J. R., Mann, G. W., Johnson, C. E., and Telford, P. J.: Constraints on aerosol processes in climate models from vertically-resolved aircraft observations of black carbon, Atmos Chem Phys, 13, 5969-5986, https://doi.org/10.5194/acp-13-5969-2013, 2013.

Kipling, Z., Stier, P., Johnson, C. E., Mann, G. W., Bellouin, N., Bauer, S. E., Bergman, T., Chin, M., Diehl, T., Ghan, S. J., Iversen, T., Kirkevag, A., Kokkola, H., Liu, X. H., Luo, G., van Noije, T., Pringle, K. J., von Salzen, K., Schulz, M., Seland, O., Skeie, R. B.,
660 Takemura, T., Tsigaridis, K., and Zhang, K.: What controls the vertical distribution of aerosol? Relationships between process sensitivity in HadGEM3-UKCA and inter-model variation from AeroCom Phase II, Atmos Chem Phys, 16, 2221-2241, https://doi.org/10.5194/acp-16-2221-2016, 2016.

Koch, D. and Del Genio, A. D.: Black carbon semi-direct effects on cloud cover: review and synthesis, Atmos Chem Phys, 10, 7685-7696, https://doi.org/10.5194/acp-10-7685-2010, 2010.

Koffi, B., Schulz, M., Breon, F. M., Dentener, F., Steensen, B. M., Griesfeller, J., Winker, D., Balkanski, Y., Bauer, S. E., Bellouin, N.,
665 Berntsen, T., Bian, H. S., Chin, M., Diehl, T., Easter, R., Ghan, S., Hauglustaine, D. A., Iversen, T., Kirkevag, A., Liu, X. H., Lohmann, U., Myhre, G., Rasch, P., Seland, O., Skeie, R. B., Steenrod, S. D., Stier, P., Tackett, J., Takemura, T., Tsigaridis, K., Vuolo, M. R., Yoon, J., and Zhang, K.: Evaluation of the aerosol vertical distribution in global aerosol models through comparison against CALIOP measurements: AeroCom phase II results, J Geophys Res-Atmos, 121, 7254-7283, https://doi.org/10.1002/2015jd024639, 2016.

670 Kokhanovsky, A. A. and Rozanov, V. V.: The determination of dust cloud altitudes from a satellite using hyperspectral measurements in the gaseous absorption band, Int J Remote Sens, 31, 2729-2744, https://doi.org/10.1080/01431160903085644, 2010.

Lu, Z. D., Wang, J., Xu, X. G., Chen, X., Kondragunta, S., Torres, O., Wilcox, E. M., and Zeng, J.: Hourly Mapping of the Layer Height of Thick Smoke Plumes Over the Western US in 2020 Severe Fire Season, Front. Remote Sens., 2, 13, https://doi.org/10.3389/frsen.2021.766628, 2021.

675 Lu, Z. D., Wang, J., Chen, X., Zeng, J., Wang, Y., Xu, X. G., Christian, K. E., Yorks, J. E., Nowottnick, E. P., Reid, J. S., and Xian, P.: First Mapping of Monthly and Diurnal Climatology of Saharan Dust Layer Height Over the Atlantic Ocean From EPIC/DSCOVR in Deep Space, Geophys Res Lett, 50, 10, https://doi.org/10.1029/2022gl102552, 2023.

Marlier, M. E., DeFries, R. S., Voulgarakis, A., Kinney, P. L., Randerson, J. T., Shindell, D. T., Chen, Y., and Faluvegi, G.: El Niño and health risks from landscape fire emissions in southeast Asia, Nature Climate Change, 3, 131-136,
680 https://doi.org/10.1038/nclimate1658, 2013.

Marshak, A., Herman, J., Szabo, A., Blank, K., Carn, S., Cede, A., Geogdzhayev, I., Huang, D., Huang, L. K., Knyazikhin, Y., Kowalewski, M., Krotkov, N., Lyapustin, A., McPeters, R., Meyer, K. G., Torres, O., and Yang, Y. K.: Earth Observations from Dscovr Epic Instrument, B Am Meteorol Soc, 99, 1829-1850, https://doi.org/10.1175/Bams-D-17-0223.1, 2018.

Muller, J. P., Denis, M. A., Dundas, R. D., Mitchell, K. L., Naud, C., and Mannstein, H.: Stereo cloud-top heights and cloud fraction retrieval
685 from ATSR-2, Int J Remote Sens, 28, 1921-1938, https://doi.org/10.1080/01431160601030975, 2007.

Nanda, S., de Graaf, M., Veefkind, J. P., Sneep, M., ter Linden, M., Sun, J. Y. T., and Levelt, P. F.: A first comparison of TROPOMI aerosol layer height (ALH) to CALIOP data, Atmos Meas Tech, 13, 3043-3059, https://doi.org/10.5194/amt-13-3043-2020, 2020.

Park, S. S., Kim, J., Lee, H., Torres, O., Lee, K. M., and Lee, S. D.: Utilization of O-4 slant column density to derive aerosol layer height from a space-borne UV-visible hyperspectral sensor: sensitivity and case study, Atmos Chem Phys, 16, 1987-2006,
690 https://doi.org/10.5194/acp-16-1987-2016, 2016.

Park, S. S., Kim, J., Cho, Y., Lee, H., Park, J., Lee, D. W., Lee, W. J., and Kim, D. R.: Retrieval Algorithm for Aerosol Effective Height from the Geostationary Environment Monitoring Spectrometer (GEMS)[preprint], https://doi.org/10.5194/amt-2023-136, 04 July 2023.

Peterson, D., Hyer, E., and Wang, J.: Quantifying the potential for high-altitude smoke injection in the North American boreal forest using
695 the standard MODIS fire products and subpixel-based methods, J Geophys Res-Atmos, 119, 3401-3419, https://doi.org/10.1002/2013jd021067, 2014.

Pierangelo, C., Chedin, A., Heilliette, S., Jacquinet-Husson, N., and Armante, R.: Dust altitude and infrared optical depth from AIRS, Atmos Chem Phys, 4, 1813-1822, https://doi.org/10.5194/acp-4-1813-2004, 2004.

700 Rao, L. L., Xu, J., Efremenko, D. S., Loyola, D. G., and Doicu, A.: Hyperspectral Satellite Remote Sensing of Aerosol Parameters: Sensitivity Analysis and Application to TROPOMI/S5P, Front. Environ. Sci., 9, 16, https://doi.org/10.3389/fenvs.2021.770662, 2022.

Stein Zweers, D. C.: TROPOMI ATBD of the UV aerosol index, S5P-KNMI-L2-0008-RP: https://sentinel.esa.int/documents/247904/2476257/Sentinel-5P-TROPOMI-ATBD-UV-Aerosol-Index.pdf, last access: 17 December 2023.

Torres, O., Bhartia, P. K., Herman, J. R., Ahmad, Z., and Gleason, J.: Derivation of aerosol properties from satellite measurements of
705 backscattered ultraviolet radiation: Theoretical basis, J Geophys Res-Atmos, 103, 17099-17110, https://doi.org/10.1029/98jd00900, 1998.

Torres, O., Tanskanen, A., Veihelmann, B., Ahn, C., Braak, R., Bhartia, P. K., Veefkind, P., and Levelt, P.: Aerosols and surface UV products from Ozone Monitoring Instrument observations: An overview, J Geophys Res-Atmos, 112, https://doi.org/10.1029/2007jd008809, 2007.

710 Vandenbussche, S., Kochenova, S., Vandaele, A. C., Kumps, N., and De Maziere, M.: Retrieval of desert dust aerosol vertical profiles from IASI measurements in the TIR atmospheric window, Atmos Meas Tech, 6, 2577-2591, https://doi.org/10.5194/amt-6-2577-2013, 2013.

Veefkind, J. P., Aben, I., McMullan, K., Förster, H., de Vries, J., Otter, G., Claas, J., Eskes, H. J., de Haan, J. F., Kleipool, Q., van Weele, M., Hasekamp, O., Hoogeveen, R., Landgraf, J., Snel, R., Tol, P., Ingmann, P., Voors, R., Kruizinga, B., Vink, R., Visser, H., and
715 Levelt, P. F.: TROPOMI on the ESA Sentinel-5 Precursor: A GMES mission for global observations of the atmospheric composition for climate, air quality and ozone layer applications, Remote Sensing of Environment, 120, 70-83, https://doi.org/https://doi.org/10.1016/j.rse.2011.09.027, 2012.

Wang, J. and Christopher, S. A.: Intercomparison between satellite-derived aerosol optical thickness and PM2.5 mass: Implications for air quality studies, Geophys Res Lett, 30, https://doi.org/10.1029/2003gl018174, 2003.

720 Wang, J. and Christopher, S. A.: Mesoscale modeling of Central American smoke transport to the United States: 2. Smoke radiative impact on regional surface energy budget and boundary layer evolution, J Geophys Res-Atmos, 111, https://doi.org/10.1029/2005jd006720, 2006.

Wang, J., Christopher, S. A., Nair, U. S., Reid, J. S., Prins, E. M., Szykman, J., and Hand, J. L.: Mesoscale modeling of Central American smoke transport to the United States: 1. "Top-down" assessment of emission strength and diurnal variation impacts, J Geophys
725 Res-Atmos, 111, https://doi.org/10.1029/2005jd006416, 2006.

Wang, J., Ge, C., Yang, Z. F., Hyer, E. J., Reid, J. S., Chew, B. N., Mahmud, M., Zhang, Y. X., and Zhang, M. G.: Mesoscale modeling of smoke transport over the Southeast Asian Maritime Continent: Interplay of sea breeze, trade wind, typhoon, and topography, Atmos Res, 122, 486-503, https://doi.org/10.1016/j.atmosres.2012.05.009, 2013.

Wang, J., Roudini, S., Hyer, E. J., Xu, X. G., Zhou, M., Garcia, L. C., Reid, J. S., Peterson, D. A., and da Silva, A. M.: Detecting nighttime
730 fire combustion phase by hybrid application of visible and infrared radiation from Suomi NPP VIIRS, Remote Sensing of Environment, 237, 14, https://doi.org/10.1016/j.rse.2019.111466, 2020.

Wendisch, M., Hellmuth, O., Ansmann, A., Heintzenberg, J., Engelmann, R., Althausen, D., Eichler, H., Wuller, D., Hu, M., Zhang, Y., and Mao, J.: Radiative and dynamic effects of absorbing aerosol particles over the Pearl River Delta, China, Atmos Environ, 42, 6405-6416, https://doi.org/10.1016/j.atmosenv.2008.02.033, 2008.

735 Winker, D. M., Tackett, J. L., Getzewich, B. J., Liu, Z., Vaughan, M. A., and Rogers, R. R.: The global 3-D distribution of tropospheric aerosols as characterized by CALIOP, Atmos Chem Phys, 13, 3345-3361, https://doi.org/10.5194/acp-13-3345-2013, 2013.

Wu, L. H., Hasekamp, O., van Diedenhoven, B., Cairns, B., Yorks, J. E., and Chowdhary, J.: Passive remote sensing of aerosol layer height using near-UV multiangle polarization measurements, Geophys Res Lett, 43, 8783-8790, https://doi.org/10.1002/2016gl069848, 2016.

740 Xu, X., Wang, J., Wang, Y., and Kokhanovsky, A.: Chapter 1 - Passive Remote Sensing of Aerosol Height, in: Remote Sensing of Aerosols, Clouds, and Precipitation, edited by: Tanvir Islam, Y. H., Alexander Kokhanovsky, Jun Wang, Elsevier, Cambridge, MA, 1-22, https://doi.org/10.1016/B978-0-12-810437-8.00001-3, 2018.

Xu, X. G., Wang, J., Wang, Y., Zeng, J., Torres, O., Reid, J. S., Miller, S. D., Martins, J. V., and Remer, L. A.: Detecting layer height of smoke aerosols over vegetated land and water surfaces via oxygen absorption bands: hourly results from EPIC/DSCOVR in deep space, Atmos Meas Tech, 12, 3269-3288, https://doi.org/10.5194/amt-12-3269-2019, 2019.

Xu, X. G., Wang, J., Wang, Y., Zeng, J., Torres, O., Yang, Y. K., Marshak, A., Reid, J., and Miller, S.: Passive remote sensing of altitude and optical depth of dust plumes using the oxygen A and B bands: First results from EPIC/DSCOVR at Lagrange-1 point, Geophys Res Lett, 44, 7544-7554, https://doi.org/10.1002/2017gl073939, 2017.

Yang, Z. F., Wang, J., Ichoku, C., Hyer, E., and Zeng, J.: Mesoscale modeling and satellite observation of transport and mixing of smoke and dust particles over northern sub-Saharan African region, J Geophys Res-Atmos, 118, 12139-12157, https://doi.org/10.1002/2013jd020644, 2013.

Zeng, J., Han, Q. Y., and Wang, J.: High-spectral resolution simulation of polarization of skylight: Sensitivity to aerosol vertical profile, Geophys Res Lett, 35, https://doi.org/10.1029/2008gl035645, 2008.

Zhang, L., Li, Q. B., Gu, Y., Liou, K. N., and Meland, B.: Dust vertical profile impact on global radiative forcing estimation using a coupled chemical-transport-radiative-transfer model, Atmos Chem Phys, 13, 7097-7114, https://doi.org/10.5194/acp-13-7097-2013, 2013.